



Jackson, M. D., Blundy, J., & Sparks, R. S. J. (2018). Chemical differentiation, cold storage and remobilization of magma in the Earth's crust. *Nature*, 564(7736), 405-409. <https://doi.org/10.1038/s41586-018-0746-2>

Peer reviewed version

License (if available):  
Other

Link to published version (if available):  
[10.1038/s41586-018-0746-2](https://doi.org/10.1038/s41586-018-0746-2)

[Link to publication record in Explore Bristol Research](#)  
PDF-document

This is the accepted author manuscript (AAM). The final published version (version of record) is available online via Springer Nature at <https://doi.org/10.1038/s41586-018-0746-2> . Please refer to any applicable terms of use of the publisher.

## University of Bristol - Explore Bristol Research

### General rights

This document is made available in accordance with publisher policies. Please cite only the published version using the reference above. Full terms of use are available:  
<http://www.bristol.ac.uk/pure/about/ebr-terms>

# 1 Chemical differentiation, cold storage and remobilization of magma in the Earth's crust

2  
3 M.D. Jackson,<sup>1</sup> J. Blundy,<sup>2</sup> R.S.J. Sparks.<sup>2</sup>

4  
5 **1 Department of Earth Science and Engineering, Imperial College London, SW176AS, UK.**  
6 **2. School of Earth Sciences, University of Bristol, BS8 1RJ, UK.**  
7

8 **The formation, storage and chemical differentiation of magma in the Earth's crust is of**  
9 **fundamental importance in igneous geology and volcanology. Recent data are challenging the**  
10 **high melt fraction 'magma chamber' paradigm that has underpinned models of crustal magmatism**  
11 **for over a century, suggesting instead that magma is normally stored in low melt fraction 'mush**  
12 **reservoirs'.<sup>1-9</sup> A mush reservoir comprises a porous and permeable framework of closely packed**  
13 **crystals with melt present in the pore space.<sup>1,10</sup> However, many common features of crustal**  
14 **magmatism have not yet been explained by either the 'chamber' or 'mush' reservoir concepts.<sup>1,11</sup>**  
15 **Here we show that reactive melt flow is a critical, but hitherto neglected, process in crustal mush**  
16 **reservoirs, occurring because buoyant melt percolates upwards through, and reacts with, the**  
17 **crystals.<sup>10</sup> Reactive melt flow in mush reservoirs produces the low crystallinity, chemically**  
18 **differentiated (silicic) magmas which ascend to form shallower intrusions or erupt to the**  
19 **surface.<sup>11-13</sup> The magmas can host much older crystals, stored at low and even sub-solidus**  
20 **temperatures, consistent with crystal chemistry data.<sup>6-9</sup> Changes in local bulk composition caused**  
21 **by reactive melt flow, rather than significant increases in temperature, produce the rapid increase**  
22 **in melt fraction that remobilizes these cool- or cold-stored crystals. Reactive flow can also**  
23 **produce bimodality in magma compositions sourced from mid- to lower-crustal reservoirs.<sup>14,15</sup>**  
24 **Trace element profiles generated by reactive flow are similar to those observed in a well-studied**  
25 **reservoir now exposed at the surface.<sup>16</sup> We propose that magma storage and differentiation**  
26 **primarily occurs by reactive melt flow in long-lived mush reservoirs, rather than by the commonly**  
27 **invoked process of fractional crystallisation in magma chambers.<sup>14</sup>**

28 Magma reservoirs occur at several depths within the crust and typically grow incrementally  
29 through the intrusion of dykes or sills.<sup>1,11,13,16,17</sup> High melt fractions must sometimes be present in  
30 these reservoirs to produce eruptible, low-crystallinity magmas.<sup>1,7,8,9,13</sup> However, geophysical data  
31 suggest that reservoirs have low melt fraction even beneath active volcanoes<sup>2-5</sup> and crystal  
32 chemistry data indicate that long-term magma storage occurs at low or even sub-solidus  
33 temperature.<sup>6-9</sup> High melt fractions are therefore ephemeral, yet geochemical models typically  
34 assume differentiation occurs by crystal fractionation from low-crystallinity magmas;<sup>11,14</sup> moreover,  
35 geochronological data demonstrate that crustal magma reservoirs can be long-lived, spanning  
36 hundreds of thousands to millions of years.<sup>17-21</sup> Existing models of crustal magma storage and  
37 differentiation cannot reconcile these conflicting observations.

38 We use numerical modelling to investigate the storage and chemical differentiation of magma in  
39 crustal reservoirs. The model describes repeated intrusion of mafic to intermediate sills into the  
40 mid- to lower crust,<sup>12,13,16,21-23</sup> the associated transport of heat via conduction and advection and, in a  
41 key advance, mass transport via reactive flow of buoyant melt through the compacting crystal  
42 framework.<sup>10</sup> Transport of chemical components with the melt modifies the local bulk composition,  
43 and melt fraction changes in response to the chemical reactions that maintain local thermodynamic  
44 equilibrium. Phase behaviour is modelled using a two-component, eutectic phase diagram that,  
45 although much simplified compared to natural systems, captures the critically important impact of  
46 bulk composition on melting behaviour and the complex non-linear relationships between  
47 composition, melt fraction and permeability (see Methods).<sup>10</sup> Melting relationships obtained from  
48 the phase diagram approximate common crustal igneous systems (Extended Data Fig. 1). The  
49 concentration of an incompatible trace element is also modelled assuming a constant partition  
50 coefficient.

51 Typical results are shown in Figure 1 (see also Supplementary Video 1). In this example, 100m  
52 thick basalt (mafic) sills are intruded randomly over a depth range of 600m, initially at 18km depth

53 and then around a depth that is controlled by the density contrast between intruding magma and  
54 host mush, reflecting the evolving reservoir composition and melt fraction (see Methods). We  
55 emplace 7.8km of basalt in total, at an average rate of  $5\text{mm}\cdot\text{yr}^{-1}$  typical of crustal magmatic  
56 systems,<sup>22-24</sup> into solid crust with an initial geotherm of  $20\text{K}\cdot\text{km}^{-1}$ .<sup>21-23</sup> Our example was chosen to  
57 facilitate comparison with data from a well-studied deep crustal section.<sup>16,21</sup> The key findings are  
58 replicated over the depth range of 10-30km typical of many crustal magma reservoirs and following  
59 intrusion of intermediate as well as mafic magma, using model parameters over a wide range  
60 reasonable for such systems (see Methods and Extended Data Table 1).

61 Initially, following each sill intrusion, the melt fraction rapidly falls to zero so there is no  
62 persistent magma reservoir (Supplementary Video 1 and Extended Data Figure 2). This is the  
63 'incubation phase' of the incipient magma reservoir, observed also in models that neglect reactive  
64 flow.<sup>22,23</sup> However, in our model, chemical differentiation occurs within each intrusion before it  
65 solidifies, with more evolved melt (enriched in the incompatible trace element) accumulating at the  
66 top of the intrusion, and more refractory and depleted crystals accumulating at the base. The rapid  
67 increase in crystallinity traps the magma at the site of intrusion, but differentiation creates  
68 compositional contrasts that cause the intrusion depth to progressively increase (Supplementary  
69 Video 1 and Extended Data Figure 3a).

70 The incubation phase ends when the melt fraction is greater than zero between successive sill  
71 intrusions, whereupon a magma reservoir has formed (Figure 1a; Supplementary Video 1). Melt is  
72 now persistently present, but melt fraction remains low except for a brief period after each new  
73 intrusion (Extended Data Figure 2b). The reservoir comprises a mush, rather than a high melt  
74 fraction magma chamber. Reactive flow now significantly modifies the predicted reservoir behaviour  
75 compared to previous models.<sup>22,23</sup>

76 Buoyant melt migrates upwards through the mush, accumulating in the upper part of the  
77 reservoir because it cannot travel beyond the solidus isotherm where the melt fraction and  
78 permeability fall to zero (Supplementary Video 1). Melt composition evolves as it flows into, and  
79 reacts with, progressively cooler mush. Reactive flow reduces, or removes, early-formed  
80 compositional contrasts, so the locally varying melt fraction controls the depth of later sill intrusions,  
81 which decreases as melt migrates upwards (see Methods). This is the 'growing phase' of the  
82 reservoir.

83 The growing phase ends when melt accumulates below the solidus isotherm to form a high melt  
84 fraction (typically  $>0.7$ ) layer overlying a thick (several km), low melt fraction (typically  $<0.2$ ) mush  
85 (Figure 1b and Supplementary Video 1). The melt-rich layer contains chemically differentiated felsic  
86 magma and can grow to several 100's m in thickness. Although not captured by the model, buoyant  
87 magma in the layer will be prone to leave the reservoir to produce shallower intrusions or volcanic  
88 eruptions.<sup>25,26</sup> Once magma leaves, a new layer grows by the same mechanism (see Methods).

89 This is the 'active phase' during which the reservoir can deliver evolved, low crystallinity magma  
90 (Extended Data Figure 2b). We suggest that, although geophysical surveys are probing active  
91 reservoirs, they image only the low melt fraction mush;<sup>2-5</sup> the overlying high melt fraction layers are  
92 not observed, because they are ephemeral and/or too thin to be resolved. Geophysical detection of  
93 such a layer would suggest that magma mobilisation (and possible eruption) was imminent.<sup>7</sup>

94 When intrusion of new sills ends, reactive flow continues wherever the temperature is above the  
95 solidus but, overall, the reservoir cools. This is the 'waning phase' (Supplementary Video 1;  
96 Extended Data Figure 3b) that persists until the mush has completely solidified (Extended Data  
97 Figure 2b). If exhumed, the resulting body of rock is termed a deep crustal section of which there  
98 are several natural examples.<sup>16,21</sup>

99 During the active phase, the high melt fraction layer forms towards the top of the reservoir  
100 where the temperature is low, rather than at the highest temperature (Figure 1b). This counter-  
101 intuitive result is a consequence of reactive flow, whereby melt accumulation causes the local bulk  
102 composition to evolve towards the eutectic. Melt composition in more chemically complex systems  
103 will evolve towards other low-variance states such as cotectics, peritectics or multiple-saturation

104 points (see Methods), but the overall behaviour will be similar. A key finding here is that high melt  
105 fraction layers in crustal mush reservoirs can form in response to changes in bulk composition  
106 caused by reactive melt flow, rather than significant increases in temperature.

107 Magma in a high melt fraction layer contains c. 10% crystals (Figure 2a). These 'antecrysts' can  
108 long pre-date magma formation, because they derive from crystallisation of early sills at the top of  
109 the reservoir. Once formed, the antecrysts are stored at near- or sub-solidus temperature (i.e. 'cool'  
110 or 'cold'; Figure 2b). The local temperature gradually increases in response to ongoing intrusion of  
111 sills deeper in the reservoir and, eventually, exceeds the solidus. Soon afterwards, buoyant, evolved  
112 melt, migrating upwards through the pore-space, accumulates around these older antecrysts,  
113 causing the local melt fraction to increase rapidly and by far more than would be possible by heating  
114 alone (Figure 2b).<sup>6,7,18,27</sup> Cold mush is remobilized here not by a significant increase in temperature,  
115 but by buoyancy-driven reactive flow supplying evolved melt from deeper, more refractory parts of  
116 the reservoir, where temperature can be high but the melt fraction remain low (Figure 2c).  
117 Remobilization is primarily caused by changes in local bulk composition, rather than temperature.

118 In our example, melt accumulation forms a low crystallinity magma a few centuries after the local  
119 temperature exceeds the solidus, yet the magma contains antecrysts formed up to c. 1–1.4Ma  
120 earlier (Figure 2b). The range of antecryst ages reflects the timing of sill intrusions relative to the  
121 timing of melt accumulation. Crystal chemistry data show cool or cold storage and remobilization of  
122 older antecrysts hosted by younger felsic magma;<sup>6–9</sup> our results suggest that this could result from  
123 reactive melt flow accumulating young, felsic melt within older mush. The antecrysts are not in  
124 equilibrium with the younger melt, creating disequilibrium crystal textures such as partial resorption.  
125 Flow of buoyant melt into the high melt fraction layer will drive convective overturn and  
126 homogenisation before, or during, evacuation of magma, yielding a range of antecryst ages that may  
127 span the entire reservoir history.<sup>28</sup>

128 Magmas in the high melt fraction layers have evolved composition. Conversely, magmas in the  
129 sills shortly after intrusion have compositions close to the intruded basalt. Low crystallinity, mafic or  
130 felsic magmas can therefore leave the reservoir, but not magmas with intermediate composition.  
131 Many volcanic settings are characterised by bimodal volcanism (the 'Daly Gap'), especially in oceanic  
132 settings (hotspots and island arc environments) and continental hotspots (Figure 3a).<sup>14,15,29</sup> Our  
133 results suggest that compositional bimodality is another consequence of differentiation by reactive  
134 melt flow in mush reservoirs. However, not all systems show bimodality.<sup>30</sup> Intermediate  
135 compositions could result from magma mixing<sup>15</sup> or differentiation within multiple mush reservoirs  
136 comprising a vertically extensive magmatic system.<sup>1</sup>

137 The modelled incompatible trace element concentration in the solidified reservoir shows a  
138 characteristic pattern. Towards the base, the spiky signature produced by differentiation in each sill  
139 during the incubation phase is preserved (Figure 3b). In the upper part, the profile is smoother and  
140 shows depletion relative to the initial concentration, reflecting extraction of melt. The top shows  
141 enrichment, reflecting accumulation of melt during the growing and active phases. Data from a  
142 deep crustal section show a similar pattern (Figure 3c).<sup>16</sup> We suggest this pattern is another  
143 characteristic product of reactive melt flow in crustal mush reservoirs. Reactive melt flow at low  
144 melt fraction, rather than fractional crystallisation at high melt fraction, is the dominant mechanism  
145 controlling magma storage, accumulation and chemical differentiation in the continental crust (Fig.  
146 4).

147

## 148 References

- 149 1. Cashman, K.V., Sparks, R.S.J. & Blundy, J.D., Vertically extensive and unstable magmatic systems: A  
150 unified view of igneous processes, *Science* **355**, (2017).
- 151 2. Huang, H.H., Lin, F.C., Schmandt, B., Farrell, J., Smith, R.B. & Tsai, V.C. The Yellowstone magmatic  
152 system from the mantle plume to the upper crust, *Science* **348** (2015).

- 153 3. Paulatto, M., Annen, C., Henstock, T.J., Kiddle, E., Minshull, T.A., Sparks, R.S.J. & Voight, B. Magma  
154 chamber properties from integrated seismic tomography and thermal modeling at Montserrat.  
155 *Geochemistry, Geophysics, Geosystems* **13**, (2012).
- 156 4. Hill, G.J., Caldwell, T.G., Chertkoff, D.G., Bibby, H.M., Burgess, M.K., Cull, J.P., & Cas, R.A.F.  
157 Distribution of melt beneath Mount St. Helens and Mount Adams inferred from magnetotelluric  
158 data. *Nature Geoscience* **2**, 785–789 (2009).
- 159 5. Ward, K.M., Zandt, G., Beck, S.L., Christensen, D.H. & McFarlin, H., Seismic imaging of the  
160 magmatic underpinnings beneath the Altiplano-Puna volcanic complex from the joint inversion  
161 of surface wave dispersion and receiver functions, *Earth and Planetary Science Letters* **404** 43–  
162 53 (2014).
- 163 6. Rubin, A.E., Cooper, K.M., Till, C.B., Kent, A.J.R., Costa, F., Bose, M., Gravley, D., Deering, C., &  
164 Cole, J. Rapid cooling and cold storage in a silicic magma reservoir recorded in individual  
165 crystals, *Science*, **356** (2017).
- 166 7. Cooper K.M. & Kent A.J.R. Rapid remobilization of magmatic crystals kept in cold storage, *Nature*  
167 **506**, 480-483 (2014).
- 168 8. Szymanowski, D., Wotzlaw, J-F., Ellis, B.S., Bachmann, O., Guillong, M. and v. Quadt, A.,  
169 Protracted near-solidus storage and pre-eruptive rejuvenation of large magma reservoirs,  
170 *Nature Geoscience* **10**, 777-782 (2017).
- 171 9. Andersen, N.L., Jicha, B.R., Singer, B.S. and Hildreth, W., Incremental heating of Bishop Tuff  
172 sanidine reveals preeruptive radiogenic Ar and rapid remobilization from cold storage,  
173 *Proceedings of the National Academy of Sciences of The United States Of America* (2017).
- 174 10. Solano, J.M.S., Jackson, M.D., Sparks, R.S.J. & Blundy, J.D. Evolution Of Major And Trace Element  
175 Composition During Melt Migration Through Crystalline Mush: Implications For Chemical  
176 Differentiation In The Crust, *American Journal of Science* **314**, 895–939 (2014).
- 177 11. Glazner, A.F., Bartley, J.M., Coleman, D.S., Gray, W. & Taylor, R.Z. Are plutons assembled over  
178 millions of years by amalgamation from small magma chambers? *Geological Society of America*  
179 *Today* **14**, 4-12 (2004).
- 180 12. Sisson, T.W., Ratajeski, K., Hankins, W.B. & Glazner, A.F., Voluminous granitic magmas from  
181 common basaltic sources, *Contrib. Mineral Petrol.* **148**, 635-661 (2005).
- 182 13. Rudnick, R.L., Making continental crust, *Nature* **378**, 571-578 (1995).
- 183 14. Brenhin Keller C., Schoene B., Barbonu M., Samperton, K.M. & Husson, J.M. Volcanic–plutonic  
184 parity and the differentiation of the continental crust, *Nature* **523**, 301-307 (2015).
- 185 15. Reubi, O. & Blundy, J. A dearth of intermediate melts at subduction zone volcanoes and the  
186 petrogenesis of arc andesites, *Nature* **461**, 1269-1273 (2009).
- 187 16. Voschage, H., Hofmann, A.W., Mazzucchelli, M., Rivalenti, G., Sinigoi, S., Raczek, I. & Demarchi,  
188 G. Isotopic evidence from the Ivrea Zone for a hybrid lower crust formed by magmatic  
189 underplating, *Nature* **347**, 731-736 (1990).
- 190 17. Coleman, D.S., Gray, W. & Glazner, A.F. Rethinking the emplacement and evolution of zoned  
191 plutons: Geochronologic evidence for incremental assembly of the Tuolumne Intrusive Suite,  
192 California. *Geology* **32**, 433–436 (2004).
- 193 18. Barboni, M., Boehnke, P., Schmitt, A.K., Harrison, T.M., Shane, P., Bouvier, AS, & Baumgartner, L.  
194 Warm storage for arc magmas, *Proceedings of the National Academy of Sciences of The United*  
195 *States Of America* **113**, 13959-13964 (2016).
- 196 19. Deering C.D., Keller, B., Schoene, B., Bachmann, O., Beane, R. & Ovtcharova, O., Zircon record of  
197 the plutonic-volcanic connection and protracted rhyolite melt evolution. *Geology* **44**, 267–270  
198 (2016).
- 199 20. Frazer, R.E., Coleman, D.S. & Mills, R.D. Zircon U-Pb geochronology of the Mount Givens  
200 Granodiorite: Implications for the genesis of large volumes of eruptible magma. *Journal of*  
201 *Geophysical Research: Solid Earth* **119**, 2907-2924 (2014).

- 202 21. Peressini, G., Quick, J.E., Sinigoi, S., Hofmann, A.W. & Fanning, M. Duration of a Large Mafic  
203 Intrusion and Heat Transfer in the Lower Crust: a SHRIMP U-Pb Zircon Study in the Ivrea-  
204 Verbanco Zone (Western Alps, Italy). *Journal of Petrology* **48**, 1185–1218 (2007).
- 205 22. Annen, C., Blundy, J.D. & Sparks, R.S.J. The Genesis of Intermediate and Silicic Magmas in Deep  
206 Crustal Hot Zones. *Journal of Petrology* **47**, 505-539 (2006).
- 207 23. Karakas, O., Degruyter, W., Bachmann, O. & Dufek, J. Lifetime and size of shallow magma bodies  
208 controlled by crustal-scale magmatism, *Nature Geoscience* **10**, 446-450 (2017)
- 209 24. Crisp, J.A., Rates of magma emplacement and volcanic output: *Journal of Volcanology and*  
210 *Geothermal Research* **20** 177 (1984).
- 211 25. Malfait, W.J., Seifert, R., Petitgirard, S., Perrillat, J.-P., Mezouar, M., Ota, T., Nakamura, E., Lerch,  
212 P. & Sanchez-Valle, C. Supervolcano eruptions driven by melt buoyancy in large silicic magma  
213 chambers. *Nature Geoscience* **7**, 122–125 (2014).
- 214 26. Keller, T., May, D.A. & Kaus, B.J.P., Numerical modelling of magma dynamics coupled to tectonic  
215 deformation of lithosphere and crust. *Geophysical Journal International* **195**, 1406-1442 (2013).
- 216 27. Huber, C., Bachmann, O. & Dufek, J., The limitations of melting on the reactivation of silicic  
217 mushes, *Journal of Volcanology and Geothermal Research* **195**, 97-105 (2010).
- 218 28. Bergantz, G.W., Schleicher, J.M. & Burgisser, A., Open-system dynamics and mixing in magma  
219 mushes, *Nature Geoscience* **8**, 793-796 (2015).
- 220 29. Ellis, B.S., Wolff, J.A., Boroughs, S., Mark, D.F., Starkel, W.A. & Bonnischen, B., Rhyolitic volcanism  
221 of the central Snake River Plain: a review, *Bull. Volcanol.* **75**, 745 (2013).
- 222 30. Bachmann, O. & Huber, C., Silicic magma reservoirs in the Earth’s crust, *American Mineralogist*  
223 **101**, pages 2377–2404, 2016.

224

#### 225 **Acknowledgements**

226 MDJ and JB acknowledge funding from NERC Grant NE/P017452/1 “From arc magmas to ores  
227 (FAMOS): A mineral systems approach”. This paper is FAMOS contribution F05. MDJ also  
228 acknowledges sabbatical support from the Department of Earth Science and Engineering, Imperial  
229 College London, during which part of the research reported here was undertaken. RSJS  
230 acknowledges support from a Leverhulme Trust Emeritus Fellowship.

231

#### 232 **Author Contribution Statement**

233 MDJ wrote the code and produced the numerical results. JB prepared the phase equilibria model  
234 and calibrated this to experimental data. RSJS provided information on context and background for  
235 the study. All authors jointly designed the numerical experiments presented and drafted the  
236 manuscript text. MDJ prepared the figures.

237

#### 238 **Author Information**

239 Reprints and permissions information is available at [www.nature.com/reprints](http://www.nature.com/reprints). The authors have no  
240 competing financial and/or non-financial interests to declare in relation to the work described.  
241 Correspondence and requests for materials should be addressed to [m.d.jackson@imperial.ac.uk](mailto:m.d.jackson@imperial.ac.uk).

#### 242 **Main Figure Legends**

243

244 **Figure 1 | Snapshots showing temperature, melt fraction, bulk composition and incompatible**  
245 **trace element concentration as a function of depth during the growing and active phases of the**  
246 **reservoir after a, 0.97Ma following the onset of sill intrusions and b, 1.39Ma. Snapshots taken from**  
247 **Supplementary Video 1. At early times (not shown; see Extended Data Fig. 3a), during the**  
248 **incubation phase, individual sills cool rapidly. At later times a, during the growing phase, a**  
249 **persistent mush reservoir forms but the melt fraction is low. Buoyant melt migrates upwards and**  
250 **begins to accumulate at the top of the mush. During the active phase b, the accumulating melt**  
251 **forms a high melt fraction layer containing mobile magma. The composition of the melt in the layer**

252 is evolved and enriched in incompatible trace elements. Elsewhere in the mush, the melt fraction  
253 remains low. At late times (not shown; see Extended Data Fig. 3b) during the waning phase, sill  
254 intrusions cease and the mush cools and solidifies. To illustrate the key processes, intruding basalt  
255 and crust are assumed in this example to have the same initial incompatible trace element  
256 concentration. Shaded area in all plots denotes the vertical extent of basalt intrusions at that time.  
257 Equivalent results for sill intrusions at 10km depth are shown in Extended Data Fig. 5.

258

259 **Figure 2 | Cold storage and rapid remobilization of magma.** Plot **a** shows melt fraction as a function  
260 of depth at three different snapshots in time (1.346Ma and 4ka before and after). Reactive flow of  
261 buoyant melt produces a high melt fraction layer that migrates upwards. Plot **b** shows temperature  
262 and melt fraction as a function of time at a depth of 18.2km, close to the top of the reservoir. Similar  
263 results are obtained over the depth range 18-18.5km. Early sill intrusions rapidly cool and crystallize.  
264 The crystals are kept in 'cold storage' at sub-solidus temperature, but the temperature gradually  
265 increases in response to sill intrusions deeper in the reservoir. Soon (<0.3ka) after the temperature  
266 exceeds the solidus, the high melt fraction layer arrives at this depth (coloured arrow denotes the  
267 corresponding snapshot in plot a) and the reservoir is remobilised: the melt fraction increases  
268 rapidly to form a low crystallinity magma. The melt fraction increases much more rapidly and to a  
269 higher value than would be possible by melting alone. Plot **c** shows temperature and melt fraction as  
270 a function of time at a depth of 20km. Similar results are obtained over the depth range 18.5-  
271 21.5km. Melt fraction remains low because reactive flow has left a refractory residue at this depth.  
272 There is no remobilization, despite the increase in temperature. Data extracted from Supplementary  
273 Video 1. Equivalent results for intrusion at 10km depth are shown in Extended Data Fig. 6.

274

275 **Figure 3 | Geochemical consequences of reactive melt flow in crustal magma reservoirs.** Plot **a**  
276 shows SiO<sub>2</sub> content of low crystallinity (crystal fraction <30%) magmas. Solid curves show bulk  
277 magma composition (melt+crystals); dashed curves show melt composition alone. The peak at low  
278 SiO<sub>2</sub> corresponds to magma within the intruding sills; the peak at high SiO<sub>2</sub> corresponds to magma  
279 within high melt fraction layers near the top of the reservoir. Also shown for comparison are data  
280 from the Snake River Plain.<sup>29</sup> The bimodality is clear, although the basalt has a lower SiO<sub>2</sub> content  
281 than modelled here. Results for different intruding sill compositions are shown in Extended Data  
282 Figure 7. Plots **b** and **c** show modelled and observed neodymium concentration along a paleo-  
283 vertical transect through the Upper Mafic Complex in the Ivrea-Verbano zone. LBZ denotes Lower  
284 Basal Zone, IBZ denotes Intermediate Basal Zone, UBZ denotes Upper Basal Zone, MG denotes Main  
285 Gabbro and DIO denotes Diorite.<sup>16</sup> Both modelled (b) and observed<sup>16</sup> (c) data show a spiky profile at  
286 the base of the reservoir, depletion in the middle part of the reservoir, and enrichment at the top.

287

288 **Figure 4 | Reactive flow of buoyant melt at low melt fraction** is a critical mechanism controlling  
289 magma storage, accumulation and differentiation in mid- to lower-crustal reservoirs. The middle  
290 and lower parts of the reservoir comprise a thick (order km) mush layer, with low and relatively  
291 uniform melt fraction, formed by early sill intrusions during the incubation and growing phases. This  
292 layer is typically imaged in geophysical data. During the active phase, the upper part of the reservoir  
293 comprises transient layers containing either intermediate/mafic, or felsic magma, that can feed  
294 shallower intrusions or surface eruptions. The felsic magma layer is formed in response to changes  
295 in local bulk composition caused by upwards reactive flow of buoyant melt through the mush. The  
296 evolved melt accumulates around older antecrysts, which may have formed during the earliest sill  
297 intrusions and hence long pre-date magma formation. In the schematic shown here, the felsic  
298 magma hosts a mixture of old and young antecrysts. The old antecrysts were formed during early sill  
299 intrusions; the young antecrysts formed during late sill intrusion at similar depth.

300

## 301 **Methods**

### 302 **Model Formulation**

303 To understand processes within crustal mush reservoirs, a quantitative model is required that  
304 includes three key features. First, the model must include the addition of hot magma or heat, to  
305 initially solid crust, in order to create and grow the reservoir.<sup>22,23,31-34</sup> Second, the model must include  
306 the relative motion of melt and crystals, to allow chemical differentiation.<sup>10,34-37</sup> Third, the model must  
307 operate primarily at low melt fraction, consistent with a wealth of evidence that crustal magma  
308 reservoirs are normally low melt fraction mushes rather than high melt fraction magma chambers.<sup>1-  
309 9,38,39</sup> At low melt fraction, a magma reservoir comprises a mush of crystals forming a solid framework  
310 with melt distributed along grain boundaries.<sup>1,10,39-41</sup> At higher melt fraction, the reservoir comprises  
311 a slurry of melt containing suspended crystals that can flow via fractures, faults or other pathways to  
312 be intruded at shallower depths or erupt at the surface.<sup>1,26,39,40</sup> The latter process is not modelled  
313 explicitly in this study.

314 The intrusion of magma to form sills can occur in numerous tectonic settings, providing both a  
315 source of heat and a source of magma that can differentiate to produce evolved melt.<sup>1,13,16,17,21-23,31-33</sup>  
316 Here, we follow earlier numerical approaches and model the repetitive intrusion of sills into the mid-  
317 to lower-crust (modelling magma reservoirs at depths over the range 10-30km), consistent with  
318 numerous contemporary magma reservoirs imaged in geophysical data, and magma reservoirs  
319 interpreted in deep crustal sections.<sup>2-5,16,21-23,31-34,42-44</sup> It is assumed that the magma in the sills is  
320 delivered from some deeper reservoir in the crust or upper mantle. In most of the example cases  
321 shown, the intruding magma is mantle-derived basalt, recognizing that crustal magmatism is largely  
322 driven by basalt<sup>13</sup> and consistent with numerous natural examples.<sup>16,21,23,42-44</sup> However, in a later  
323 section we also show results for a case when the intruding sills contain more evolved (intermediate)  
324 magma.

325 Most models of repetitive sill intrusion do not include relative motion of melt and crystals and,  
326 therefore, there is no chemical differentiation: the bulk composition of the mush reservoir remains  
327 constant.<sup>22,23,31-33</sup> Here, it is assumed that melt within the mush reservoir, produced by cooling and  
328 crystallisation of the intruded sills and also heating and melting of the surrounding crust, is present  
329 along grain boundaries and forms an interconnected network at low melt fraction.<sup>10,39-41</sup> The melt is  
330 buoyant because it is less dense than the surrounding crystals, so a pressure gradient is present which  
331 causes upwards flow of melt relative to the crystalline matrix.<sup>10,34,39</sup> The matrix can deform in response  
332 to melt flow.<sup>45-47</sup> This coupled process of melt migration and matrix deformation is termed  
333 compaction.<sup>48</sup> There is abundant evidence that compaction occurs in a wide variety of crustal igneous  
334 systems, and our assumptions are consistent with previous models of compaction.<sup>10,26,34,48-52</sup>

335 Melt flow along grain boundaries in a mush reservoir allows efficient exchange of heat and mass  
336 between melt and solid phases, so that in most of the mush and over most of its lifetime, the phases  
337 remain in local thermal and chemical equilibrium.<sup>53</sup> The local bulk composition of the mush therefore  
338 changes as the melt migrates upwards and the crystals compact downwards. To capture this, our  
339 model includes component transport and chemical reaction.<sup>10,36,37,54</sup> The results shown here  
340 demonstrate that reactive flow of melt is a critically important process controlling the storage,  
341 accumulation and chemical evolution of magma within the mush reservoir.

### 342 **Governing equations and method of solution**

343 The governing equations and method of solution are modified from Solano et al.<sup>10</sup> The enthalpy  
344 method is used to describe conservation of heat<sup>55</sup> and a binary eutectic phase diagram is used to  
345 describe solid and melt compositions assuming local thermodynamic equilibrium.<sup>10,37</sup>

346 In common with many previous studies, compaction is modelled using a modified version of the  
347 McKenzie formulation,<sup>48</sup> assuming that deformation of the matrix occurs by melt-enhanced diffusion  
348 creep.<sup>45-47</sup> This is reasonable in supra-solidus mush reservoirs deforming at low strain rates ( $\ll 10^{-15} \text{ s}^{-1}$ )  
349 and yields a Newtonian rheology for the mush.<sup>56</sup> The matrix shear viscosity is assumed constant,  
350 but the matrix bulk viscosity has a power-law relationship with melt fraction.<sup>26,50,57</sup> The melt is also



352 assumed to have a Newtonian rheology, which is reasonable for crystal-free melts containing a few  
 353 wt% water.<sup>57,58</sup>

354 Surface tension and interphase pressure are neglected. The compaction formulation is currently  
 355 being extended to include these potentially important effects, but a single, self-consistent model that  
 356 includes phase change has not yet been presented.<sup>59-63</sup> Differential stresses imposed by tectonic  
 357 forces, and magma chamber over-pressuring and loading<sup>64</sup> are also neglected, recognizing that at least  
 358 some grain boundary flow is essential to separate melt and crystals in a mush reservoir and buoyancy  
 359 is always available to drive this. Volatiles are assumed to remain in solution, so are not present as a  
 360 separate phase. In shallow crustal reservoirs, an exsolved volatile phase likely plays an important role  
 361 in controlling phase relations and melt flow, and driving magma mobilization.<sup>65,66</sup>

362 As outlined in Solano et al.,<sup>10</sup> the transport of heat, mass and components is modelled in 1-D,  
 363 using a continuum formulation of the governing conservation equations. Typical sill intrusions and  
 364 crustal mush reservoirs have high aspect ratio.<sup>2-5,16,21,38,42-44,67,68</sup> Given this, and the predominately  
 365 vertical flow of buoyant melt in the mush, a 1-D model is a reasonable starting point to determine the  
 366 effects of reactive melt flow on magma storage and differentiation. However, a 1-D model does not  
 367 admit the formation of high porosity, sub-vertical channels caused by reactive infiltration instability.<sup>54</sup>  
 368 Numerical modelling in 2-D has suggested that such channels are created during reactive melt flow in  
 369 the mantle,<sup>54,69,70</sup> but their formation and significance in crustal mush reservoirs is not yet clear.  
 370 Future work should investigate whether additional and important controls on flow in crustal magma  
 371 reservoirs are observed in 2- and 3-D models. Such models are likely to be computationally expensive.

372 The Boussinesq approximation is applied, so density differences between solid and liquid are  
 373 neglected except for terms involving gravity.<sup>10,34,51</sup> Melt fraction and porosity are synonymous in this  
 374 model. However, in contrast to previous models of crustal magma reservoirs, changes in local bulk  
 375 composition resulting from melt migration mean that the local melt fraction here cannot be simply  
 376 related via temperature to the melt fraction in the initial bulk composition (Extended Data Fig. 1c).  
 377 This is a very important aspect of our model and one that pertains in both simple chemical systems  
 378 (as employed here) and complex natural systems.

379 The governing equations can be expressed in dimensionless form as<sup>10</sup>

$$380 \quad \frac{\partial h'}{\partial t'} = \kappa \frac{\partial^2 T'}{\partial z'^2} + Ste \frac{\partial}{\partial z'} \left( (1-\phi) w'_s \right) \quad (1)$$

$$381 \quad \frac{\partial C}{\partial t'} = - \frac{\partial}{\partial z'} \left( (1-\phi) w'_s C_s \right) - \frac{\partial}{\partial z'} \left( \phi w'_m C_m \right) \quad (2)$$

$$382 \quad \frac{\partial I}{\partial t'} = - \frac{\partial}{\partial z'} \left( (1-\phi) w'_s I_s \right) - \frac{\partial}{\partial z'} \left( \phi w'_m I_m \right) \quad (3)$$

$$383 \quad \frac{\partial}{\partial z'} \left( \phi^{-\beta} \frac{\partial w'_s}{\partial z'} \right) = \frac{\mu' w'_s}{\phi^\alpha} + (1-\phi) \Delta \rho' \quad (4)$$

$$384 \quad \phi w'_m = -(1-\phi) w'_s \quad (5)$$

385 where  $h$  is enthalpy per unit mass;  $T$  is temperature;  $t$  is time;  $z$  is the vertical coordinate;  $w$  is velocity;  
 386  $\phi$  is melt fraction;  $C$  is composition, defined using the phase diagram described in the next section;  $I$  is  
 387 trace element concentration;  $\Delta \rho$  is the density contrast between melt and crystals and  $\mu$  is melt shear  
 388 viscosity, both discussed in the next section. Subscripts  $s$  and  $m$  denote solid and melt, respectively.  
 389 Primes denote the dimensionless equivalents of the dimensional variables.

390 The characteristic time- and length scales used to non-dimensionalize the equations are given  
 391 by<sup>10</sup>

392 
$$\tau = \frac{1}{\Delta\rho_r g} \left( \frac{\mu_r \eta_0}{a^2 b} \right)^{\frac{1}{2}} \quad (6)$$

393 
$$\delta = \left( \frac{\eta_0 a^2 b}{\mu_r} \right)^{\frac{1}{2}} \quad (7)$$

394 where  $\Delta\rho_r$  is a reference density contrast and  $\mu_r$  a reference melt shear viscosity discussed in the  
 395 next section,  $g$  is the acceleration due to gravity, and the matrix viscosity is related to the melt  
 396 fraction by<sup>10,34,50</sup>

397 
$$\frac{4}{3}\eta + \xi = \eta_0 \phi^{-\beta} \quad (8)$$

398 where  $\eta$  is the shear viscosity,  $\xi$  is the bulk viscosity,  $\eta_0$  is a reference shear viscosity and  $\beta$  is an  
 399 adjustable constant. The permeability of the mush  $k_\phi$  is given by<sup>10,34,48,51</sup>

400 
$$k_\phi = a^2 b \phi^\alpha \quad (9)$$

401 where  $a$  is the grain size, and  $b$  and  $\alpha$  are adjustable constants.

402 Temperature and enthalpy are scaled using<sup>10</sup>

403 
$$T' = \frac{T - T_S}{T_L - T_S} \quad (10)$$

404 
$$h' = \frac{h - h_S}{h_L - h_S} \quad (11)$$

405 where the subscripts  $L$  and  $S$  denote liquidus and solidus respectively. The dimensionless scaling factor  
 406  $\kappa$  in equation (1) is given by<sup>10</sup>

407 
$$\kappa = \frac{k_T \tau (T_L - T_S)}{\rho_r \delta^2 (c_p (T_L - T_S) + L_f)} \quad (12)$$

408 and the Stefan Number by<sup>10</sup>

409 
$$Ste = \frac{L_f}{c_p (T_L - T_S) + L_f} \quad (13)$$

410 where  $k_T$  is the thermal diffusivity,  $c_p$  the sensible heat capacity,  $L_f$  the latent heat of fusion and  $\rho_r$  is a  
 411 reference density discussed in the next section.

412 The initial condition is chemically homogenous crust with a constant linear geotherm  $T_{geo}$  and no  
 413 melt present. Temperature, melt fraction and velocity are zero at the upper boundary (Earth surface);  
 414 the lower boundary has constant  $T_{geo}$  and is set sufficiently deep that melt fraction and velocity remain  
 415 zero. Equations (1)-(5) were solved numerically using finite difference methods and a code developed  
 416 by the authors. Equation (1) was approximated using a forward-time-centered-space scheme;  
 417 equations (2) and (3) using a modified Lax-Wendroff scheme; and equation (4) using a centered  
 418 scheme. Node spacing and time-steps were chosen based on the results of convergence tests.  
 419 Solutions reported here used 20-40 nodes per individual sill intrusion with time steps that were always  
 420 less than the well-known CFL condition.<sup>34,71</sup>

421 The numerical methods and code have been validated extensively against analytical  
 422 solutions.<sup>10,34,51,71</sup> The energy conservation equation (1) is a special case of the general parabolic  
 423 diffusion-advection equation, while the mass conservation equations (2) and (3) are special cases of  
 424 the general hyperbolic flux conservative equation. Analytical solutions are available for simplified  
 425 forms of these general equations, and the numerical methods were tested against these. An analytical  
 426 solution is available for a simplified set of the compaction equations and the code was also tested  
 427 against this.

428

### 429 Phase behaviour and composition-dependent material properties

430 Phase change and compositions are described using a binary eutectic phase diagram that  
 431 approximates the behaviour of natural systems. Several previous studies of crustal igneous systems  
 432 have used a similar approach, which is preferable to more complex models involving, for example, the  
 433 thermodynamic software MELTS<sup>72</sup> for two reasons. First, reactive flow leads to local changes in bulk  
 434 composition, so the local phase equilibria must be recalculated at each location and time; this is trivial  
 435 using a simple phase diagram, but computationally intensive (albeit possible) using MELTS. Second, it  
 436 allows fundamental aspects of compositional evolution to be identified without the additional  
 437 complexity associated with modelling the phase behaviour of natural systems.<sup>10,37</sup>

438 Melt fraction is related to composition through

$$439 \quad \varphi = \frac{C - C_s}{C_m - C_s} \quad (14)$$

440 where  $C$  is the local bulk composition. Assuming a linear release of enthalpy during melting, enthalpy  
 441 is related to temperature through

$$442 \quad h = c_p T + L_f \varphi \quad (15)$$

443 Using equations (14) and (15), and the temperature-dependent liquid and solid compositions  
 444 determined from the phase diagram, the melt fraction is determined locally.

445 The binary eutectic phase diagram is described by a quadratic function given by<sup>10</sup>

$$446 \quad C_m = \begin{cases} \frac{-a_2 - \sqrt{a_2^2 - 4a_1(a_3 - T)}}{2a_1} & C < e \\ \frac{-b_2 + \sqrt{b_2^2 - 4b_1(b_3 - T)}}{2b_1} & C > e \end{cases} \quad (16)$$

$$447 \quad C_s = \begin{cases} 0 & C < e \\ 1 & C > e \end{cases} \quad (17)$$

448 Here, only compositions with  $C < e$  were used. Values of the constants  $a_1 - a_3$  were selected so that  
 449 the melting relations obtained for starting compositions chosen to represent crust and intruded basalt  
 450 match typical experimental data for the equilibrium melting/crystallization of metagreywackes and  
 451 basalt, respectively, over the pressure range 400 – 900MPa (Extended Data Figure 1a; Extended Data  
 452 Table 1).<sup>12,73,74</sup> The match is surprisingly good given the simple phase behaviour adopted.

453 It is important to recognize that the static melt fraction versus temperature relations shown in  
 454 Extended Data Figure 1a are specific to the chosen starting bulk compositions. They are not valid if  
 455 the bulk composition changes in response to reactive melt flow. The phase diagram provides a family  
 456 of melting curves for all bulk compositions encountered in the reservoir; we show just two in Extended  
 457 Data Fig. 1a. The effect of reactive melt flow in the reservoir is to decouple melt fraction and  
 458 temperature (Extended Data Figure 1c). High melt fraction can be found at low temperature where

459 reactive melt flow has caused the bulk composition of the mush to evolve towards the eutectic and  
 460 *vice-versa*. It is often assumed that high melt fraction necessitates high temperature.<sup>6-8,22,23,31-33,75,</sup>  
 461 Reactive melt flow means that this is not the case in crustal mush reservoirs.

462 We choose to relate composition  $C$  to a simple measure of differentiation, the  $\text{SiO}_2$  content, by

$$463 \quad S_{\text{SiO}_2} = a_5 + a_6 \tanh(a_7 + a_8 C) \quad (18)$$

464 Values of the constants  $a_5 - a_8$  were selected to yield a variation in  $\text{SiO}_2$  content with temperature that  
 465 matches melt  $\text{SiO}_2$  content from the same experimental melting/crystallization data (Extended Data  
 466 Figure 1b; Extended Data Table 1). Again, the match is surprisingly good given the simple phase  
 467 behavior adopted.

468 Rearrangement of equations (14), (16) and (17), followed by substitution into (15), yields a cubic  
 469 polynomial in melt fraction, dependent on enthalpy  $h$  and bulk composition  $C$ , which can be solved  
 470 analytically<sup>10</sup>

$$471 \quad \phi = \frac{h}{L_f} - \frac{c_p}{L_f} \left( \frac{a_3 + \left( \left( 2a_1 \left( \frac{C - C_s + C_s \phi}{\phi} \right) + a_2 \right)^2 + a_2^2 \right)}{4a_1} \right) \quad (19)$$

472 The model includes partitioning of a trace element between crystals and melt. The concentration  
 473 in the melt is given by

$$474 \quad I_m = \frac{I}{K + \phi(1 - K)} \quad (20)$$

475 and in the solid by

$$476 \quad I_s = KI_m \quad (21)$$

477 In the cases modelled here, the intruding magma and crust have the same initial concentration of an  
 478 incompatible trace element. This is unlikely in nature, but allows the evolution of trace element  
 479 concentration in response to reactive melt flow in the mush to be more clearly observed and  
 480 understood. Trace element concentration does not affect the evolution of temperature or melt  
 481 fraction, so the other key model results remain unchanged.

482 The density of the melt and matrix, and the viscosity of the melt, both vary as a function of  
 483 composition. Solid and melt densities are given by

$$484 \quad \rho_m = C\rho_{m\min} + (1 - C)\rho_{m\max} \quad (22a)$$

$$485 \quad \rho_s = C\rho_{s\min} + (1 - C)\rho_{s\max} \quad (22b)$$

486 where the subscripts max and min denote, respectively, the most evolved and least evolved (most  
 487 refractory) compositions in the system. The average density of the crystals+melt mixture (mush or  
 488 magma) is given by

$$489 \quad \bar{\rho} = \phi\rho_m + (1 - \phi)\rho_s \quad (23)$$

490 The dimensionless density is obtained by dividing by a reference density  $\rho_r$  chosen as the initial density  
 491 of the crust, and the dimensionless density contrast is obtained by dividing by a reference density

492 contrast  $\Delta\rho_r$  chosen to be the difference in density between the most refractory crystals ( $\rho_{smax}$ ) and  
493 most evolved melt ( $\rho_{mmin}$ ).

494 The logarithm of melt shear viscosity  $\mu$  is linearly related to the dimensionless silica content of  
495 the melt  $s_{SiO_2}$

$$496 \quad \mu = 10^{((\mu_{max} - \mu_{min})S_{SiO_2} + \mu_{min})} \quad (24)$$

497 with

$$498 \quad s_{SiO_2} = \frac{S_{SiO_2} - S_{SiO_2}^{min}}{S_{SiO_2}^{max} - S_{SiO_2}^{min}} \quad (25)$$

499 where  $S_{SiO_2}$  is the silica content of the melt (wt%).<sup>58</sup> The dimensionless melt shear viscosity is then  
500 obtained by dividing by a reference viscosity  $\mu_r$  chosen to be the maximum melt viscosity in the system  
501 (corresponding to the most evolved composition), to yield

$$502 \quad \mu' = 10^{(\log(\mu_{min}/\mu_{max})(1 - s_{SiO_2}))} \quad (26)$$

503 In the illustrative models shown here, melt viscosity varies from a minimum of 1 Pa·s to a maximum  
504 of 10<sup>5</sup> Pa·s (Extended Data Table 1) for the most mafic and felsic compositions respectively, which is  
505 reasonable for melt containing a few wt% water.<sup>58</sup> A range of maximum melt viscosities is investigated  
506 in the sensitivity analysis described below.

507

#### 508 **Modelling of sill intrusion**

509 The governing equations do not include terms representing addition of heat and mass in response to  
510 repetitive sill intrusion. Each sill intrusion is modelled numerically, using a simple approach in which  
511 new nodes, populated with the properties (enthalpy, melt fraction, major element composition and  
512 trace element concentration) of the magma in the sill, are added into the model at the target intrusion  
513 depth.<sup>22,32,34</sup> The number of new nodes is chosen to yield the desired sill thickness. Pre-existing nodes  
514 below the location of sill intrusion are shifted downwards to accommodate the new nodes  
515 representing the sill; this approach represents, numerically, the case that intrusion of each new sill  
516 causes downwards displacement of deeper crust and approximates isostatic equilibrium. Intrusion of  
517 each sill is assumed to occur over a timescale that is small compared to the thermal and chemical  
518 evolution of the magma reservoir and within a single time-step in the model. We note that injection  
519 of magma may generate local over-pressure, fracturing and, during the growing and active phases of  
520 the magma reservoir, locally disrupt the mush. Future refinements will focus on methods to better  
521 couple thermal and mechanical models.

522

#### 523 **Sill intrusion depth**

524 Previous numerical studies have modelled repetitive intrusion by over-accretion, in which each new  
525 sill is intruded immediately above the previous sill; under-accretion, in which each new sill is intruded  
526 immediately below the previous sill; and random intrusion of sills and dykes around a fixed depth.<sup>21-  
527 23,32-34</sup> The approach used here to link sill intrusion depth to the state of the mush reservoir at the time  
528 of intrusion yields variations in intrusion depth that are not captured by these previous models.

529 Controls on the depth of sill intrusions include rigidity contrasts and rheology anisotropy, resulting  
530 from variations in lithology and (if present) melt fraction; rotation of deviatoric stress such that the  
531 minimum deviatoric stress becomes vertical; and density contrasts between the surrounding country  
532 rock and intruding magma.<sup>67,68</sup> The initial intrusion depth is chosen here to match the depth of an  
533 observed magma reservoir. Understanding why a sill should be initially emplaced at a given depth is  
534 beyond the scope of the paper. Once the first sill is emplaced, the depth of subsequent intrusions is

535 controlled by the density contrast between the intruding magma and the surrounding reservoir. The  
536 next sill intrusion occurs at the deepest level of the mush that has a lower bulk density (crystals + melt)  
537 than the intruding magma. The top of the resulting reservoir tends to be close to the initial intrusion  
538 depth.

539 Density contrasts are controlled by the local composition and/or melt fraction of the mush  
540 reservoir. We use density contrasts here as a proxy for rigidity contrasts resulting from changes in  
541 rock composition or mush melt fraction.<sup>21,56,57,67,68</sup> Density is calculated using equations (22) and (23);  
542 the chosen values of density for refractory crystals ( $\rho_{\text{ymax}}$ ) and most evolved melt ( $\rho_{\text{min}}$ ) (Extended  
543 Data Table 1) yield densities of c.3000kg·m<sup>-3</sup> and c.2600kg·m<sup>-3</sup> for solid basalt and evolved (felsic) rock  
544 compositions respectively, and densities of c.2800kg·m<sup>-3</sup> and c.2350kg·m<sup>-3</sup> for their corresponding  
545 molten counterparts. These values are consistent with measured data.<sup>25,76,77</sup> The initial (reference)  
546 density of the solid crust is c.2850kg·m<sup>-3</sup>, consistent with data for intermediate rocks.<sup>77</sup>

547 During the incubation phase, melt fraction falls to zero between successive sill intrusions (Extended  
548 Data Figure 2), but variations in density arise in response to differentiation within each intruded sill as  
549 it cools. Differentiation yields a lower density, evolved top and a higher density, more refractory base  
550 (Extended Data Figure 3a and Supplementary Video 1). Similar compositional trends are observed in  
551 sills now exposed at the surface.<sup>10,78,79</sup> The density-controlled intrusion depth of each new sill is,  
552 therefore, located below the deepest evolved top of a previous, now solidified, sill intrusion.

553 During the growing and active phases of the reservoir (Extended Data Figure 2b), melt is  
554 persistently present and the compositional and density variations formed during the incubation phase  
555 are reduced by reactive melt flow (Figure 1 and Supplementary Video 1). Variations in density are  
556 then primarily controlled by melt fraction, so the density-controlled intrusion depth of each new sill is  
557 located below the deepest high melt fraction layer.

558 Field observations from deep crustal sections suggest that intrusions progressively accumulate to  
559 form a mush zone.<sup>16,21,76</sup> At early times, when the heat content of the reservoir is still low, intrusions  
560 cool without causing significant melting of the surrounding crust, leaving septa of crust interleaved  
561 with the intruded sills. We model this by intruding sills at random over a range of 300m above and  
562 below the intrusion depth determined by density contrast.

563 Random intrusion preserves septa of crustal rock between sill intrusions, whereas strictly density-  
564 controlled intrusion does not (see also Solano et al.<sup>10</sup>). Varying the depth range of random intrusion  
565 affects the frequency and volume of preserved septa, but does not otherwise affect significantly the  
566 results obtained. Although septa between early intrusions are preserved, septa between later  
567 intrusions, when the heat content of the reservoir is higher, are partially assimilated into the melt  
568 phase, causing crustal contamination of the melt.<sup>16,76,80-81</sup>

569

### 570 **Validity of the model at high melt fraction**

571 The reactive flow and compaction formulation is applied in the model regardless of local melt  
572 fraction. However, it is strictly valid only when the crystals form a solid framework that will expel melt  
573 if it undergoes mechanical disruption or viscous deformation.<sup>82</sup> Estimates of the melt fraction at which  
574 this framework forms vary widely (over the range c. 0.4 - 0.7) and likely depend on local shear stresses  
575 and strain rates, and the crystal morphology and size distribution.<sup>40,45,82-84</sup> Melt fractions higher than  
576 this are present in each sill immediately after intrusion and in the melt layers that form in response to  
577 reactive flow. However, we argue below that the formulation captures enough of the physics to yield  
578 informative results.

579 High melt fractions are present in the intruding sills over very short timescales (of order 100's years)  
580 because the sills cool very rapidly, losing heat to the surrounding reservoir and/or crust (e.g. Extended  
581 Data Figure 2a). Over these short timescales following each intrusion, crystal-melt separation is  
582 assumed in the model to occur only by reactive flow and compaction, omitting other mechanisms of  
583 crystal-melt separation;<sup>82</sup> moreover, it is assumed that there is no bulk flow of melt+crystals driven by  
584 convection.<sup>28,85,86</sup> However, the modelled cooling timescale is correct, because the rate of heat loss  
585 from each sill is dominated by conduction and this is described by equation (1).<sup>71,86</sup> Furthermore, in

586 each sill, the model captures enough crystal/melt separation to yield a more evolved top, relatively  
587 enriched in incompatible trace elements, and a more refractory base, relatively depleted in  
588 incompatible trace elements, consistent with observations (e.g. Figure 3).<sup>10,78,79</sup>

589 High melt fractions are also present in the layers that form in response to reactive melt flow (e.g.  
590 Figure 1). These layers are persistently present once formed and the model again assumes crystal-  
591 melt separation in each layer occurs only by reactive flow and compaction and that there is no bulk  
592 flow of melt+crystals driven by convection. However, the rate of delivery of new melt into the layer  
593 is controlled by reactive flow and compaction of the underlying mush where the formulation is valid.  
594 Moreover, the rate of upwards movement of the layer, which affects cold storage, is controlled by the  
595 rate of upwards movement of the solidus isotherm; this depends on conductive heat transfer in the  
596 overlying mush and solid rock, and is captured by the formulation. Thus we argue that the model  
597 captures the overall growth and upwards migration of the layers.

598 Within each high melt fraction layer, the formulation likely does not correctly capture the  
599 variation in melt fraction. However, the modelled temperature in each layer is constant at the solidus;  
600 melt fraction is also high and approximately constant, controlled primarily by the local bulk  
601 composition (e.g. Extended Data Video 1; Figure 1). Thus, the modelled temperature and melt fraction  
602 assuming reactive flow with no bulk flow of melt+crystals are similar to what would be observed for  
603 the opposite end-member model of vigorous convection in which crystals are suspended and mixed  
604 in the magma.<sup>28</sup> We argue that vigorous convection may be more likely given the results of earlier  
605 studies of single sill intrusions.<sup>28,85,86</sup>

606

#### 607 **Magma mobilisation**

608 Accumulation of melt creates a high melt fraction layer which, as it migrates upwards, can remobilize  
609 old mush by causing a rapid increase in melt fraction. The short timescale of this process may not  
610 allow for local chemical equilibrium to be maintained, so older crystals can be preserved in the  
611 younger magma. Disequilibrium between melt and crystals may also give rise to resorption and  
612 zonation of crystals which is not described here.

613 The model does not attempt to capture migration out of the reservoir of the high melt fraction  
614 (low crystallinity) magmas in the layer. Felsic magma that accumulates at the top of the reservoir is  
615 buoyant relative to the surrounding mush reservoir, so there is a pressure gradient to drive ascent to  
616 higher crustal levels or eruption at the surface.<sup>25,26</sup> The magma in each sill also evolves during cooling  
617 to become more buoyant relative to the more refractory mush, which may drive ascent of less evolved  
618 magmas. Preliminary work, not reported here, suggests that removal of felsic magma accumulating  
619 in a high melt fraction layer at the top of the reservoir does not affect the formation of subsequent  
620 layers, so long as ongoing sill intrusions continue to supply new magma to the reservoir.

621 This preliminary work is not reported because the model does not yet include clearly defined  
622 criteria for magma removal and ascent. Moreover, we note that the presence of volatile species, such  
623 as H<sub>2</sub>O, whose solubility is pressure-dependent, complicates phase relations and physical properties  
624 during magma ascent, and consequently is not considered here. Further work should determine the  
625 controls on mobilization and eruption of the low crystallinity magmas present in crustal mush  
626 reservoirs. What is clear from the results obtained here is that the compositions of low crystallinity  
627 magmas that can leave the reservoir, regardless of how or why that happens, are bimodal. In our  
628 model, the melt composition evolves to the eutectic; in more chemically complex systems, melt  
629 composition will evolve to other low-variance states, such as cotectics or peritectics (reaction  
630 boundaries). In all cases, the effect is to buffer chemically the composition of accumulated melts, as  
631 recently suggested on the basis of phase equilibrium experiments.<sup>87</sup>

632

#### 633 **Magmatic systems at shallower depth**

634 The results shown in Figure 1 (and also Supplementary Video 1 and Extended Data Figure 3)  
635 illustrate the key processes occurring within a crustal mush reservoir and were obtained using values

636 of the model parameters that are typical of crustal systems (Extended Data Table 1 and associated  
637 references). The initial intrusion depth was chosen to allow model results to be compared against a  
638 deep crustal section now exposed at the surface: the Upper Mafic Complex of the Ivrea-Verbano  
639 zone, Italy.<sup>16,21,76</sup> The complex is interpreted to represent c.8km of basalt intruded into the crust  
640 over a few Ma (i.e. at intrusion rates of order a few mm·a<sup>-1</sup>). The top of the complex is interpreted  
641 to have been located at a depth of c.18 km at the time of formation.

642 The model results can explain a wide range of magmatic phenomena. However, we recognize that  
643 many of the magmatic systems that provide compelling evidence for these phenomena cannot be  
644 approximated by a model tuned specifically to match data from the Upper Mafic Complex. In  
645 particular, systems providing evidence for cold storage and/or compositional bimodality are often  
646 located at shallower levels in the crust.<sup>6-9</sup> Moreover, major and trace element and isotopic data for  
647 these systems suggest they may be supplied by magmas of more evolved composition than basalt.<sup>6-  
648 9,88</sup> In transcrustal magmatic systems<sup>1</sup> there are likely multiple zones of intrusion: primitive basalt  
649 magmas may form intrusions deep in the crust that generate more evolved magmas; these magmas  
650 ascend through the crust to form intrusion zones at shallower depths.

651 We test here whether similar results are obtained if the first sill is intruded at a depth of 10km,  
652 rather than 18km. Numerous magmatic systems are observed in geophysical data at similar  
653 depth.<sup>2,4,5,38</sup> All model parameters are the same as used previously (Extended Data Table 1), except  
654 that we assume the initial geotherm is appropriate for thermally mature crust where, for example, a  
655 deeper magmatic zone has thermally primed the upper crust prior to the onset of shallower  
656 magmatism. Previous studies have shown that this is necessary to allow upper crustal magmatic  
657 systems to form without a prohibitively long incubation period or unreasonably high rate of magma  
658 intrusion.<sup>23</sup>

659 The results obtained are qualitatively similar to those observed at 18km depth. There is an  
660 incubation period, during which the melt fraction rapidly falls to zero, with compositional contrasts  
661 formed by chemical differentiation within each sill intrusion prior to solidification causing the intrusion  
662 depth to increase progressively (Supplementary Video 2; Extended Data Figure 4a). During the  
663 growing phase, buoyant melt again migrates upwards through the mush and reactive melt flow  
664 reduces, or removes, early formed compositional contrasts, so that the intrusion depth becomes  
665 controlled by the locally varying melt fraction (Supplementary Video 2; Extended Data Figure 5a).

666 During the active phase, the reservoir can again produce evolved, low crystallinity magmas from  
667 the high melt fraction layer that forms beneath the solidus isotherm, close to the top of the reservoir  
668 (Supplementary Video 2; Extended Data Figure 5b). When intrusion of new sills ends, the reservoir  
669 enters the waning phase (Supplementary Video 2; Extended Data Figure 4b) until the mush has  
670 completely solidified.

671 Cold storage is again observed where upwards migrating, evolved melt rapidly accumulates around  
672 older antecrysts derived from crystallisation of early sills (Extended Data Figure 6). In this shallower  
673 example, melt accumulation forms a low crystallinity magma a few 100's years after the local  
674 temperature exceeds the solidus, but the magma contains antecrysts formed c. 1.3Ma earlier  
675 (Extended Data Figure 6). Compositional bimodality is again observed, as magmas in the high melt  
676 fraction layers have evolved composition, but magmas in the sills shortly after intrusion have  
677 compositions close to that of the intruded basalt (Extended Data Figure 7a). Thus, the key results are  
678 consistently observed in models of shallower magmatic systems created and sustained by basaltic  
679 magmatism.

680

### 681 **Intrusion of more evolved magma**

682 We now test whether similar results are obtained at 10km if the intruding sills contain magma of  
683 intermediate (andesitic) rather than basaltic composition. All other model parameters are the same  
684 as used in the previous 10km model (Extended Data Table 1). We do not model intrusion of rhyolite  
685 magma because our density controlled intrusion depth model does not apply for rhyolite magma:



686 density controlled intrusion alone would suggest that rhyolite should mostly erupt. That evolved, low  
687 density magmas often intrude rather than erupt has been a challenge to density driven models of  
688 magma ascent and intrusion for many years.<sup>67,68</sup>

689 Intrusion of intermediate composition (c. 61% SiO<sub>2</sub>) magma yields qualitatively similar behavior to  
690 that observed in response to intrusion of basaltic magma. The incubation, growing, active and waning  
691 phases of reservoir life are all observed and, during the active phase, a high melt fraction layer  
692 containing evolved (felsic) magma overlies a thicker, low melt fraction mush (e.g. Extended Data  
693 Figure 8). Older antecrysts are again rapidly remobilized by the arriving melt layer although, in this  
694 case, storage is ‘cool’ rather than ‘cold’: the temperature remains above the solidus, but the melt  
695 fraction remains low until the melt layer arrives. Whether crystals are kept in cold (sub-solidus) or  
696 cool (supra-solidus) conditions may be difficult to determine from crystal chemistry data, requiring  
697 accurate estimates of reservoir and solidus temperatures;<sup>6-9</sup> the key point is that the crystals are  
698 stored at low (non-eruptible) melt fraction, as opposed to ‘warm storage’ where the magma remains  
699 eruptible.<sup>18</sup>

700 Compositional bimodality is again observed, but here the magma compositions are either evolved  
701 (felsic), reflecting melt accumulation in the upwards migrating layer, or intermediate, reflecting the  
702 composition of the intruding magma (Extended Data Figure 7b). In general, we suggest that crustal  
703 mush reservoirs deliver magmas with compositions that reflect either (i) low-variance states, such as  
704 eutectics, cotectics or peritectics (reaction boundaries)<sup>87</sup> or (ii) the intruding magma that creates the  
705 reservoir.

706

#### 707 **Intrusion depth model**

708 Numerical tests show that compositionally bimodal, low crystallinity magmas are obtained regardless  
709 of whether the intrusion depth is modelled using our sill intrusion depth model or simple under- or  
710 over-accretion. ‘Cold’ (or at least ‘cool’) storage of crystals, in a non-eruptible state, is also observed  
711 (e.g. Extended Data Figure 9a,b), except when intrusion depth is modelled using simple over-accretion.  
712 Over-accretion cannot yield cold or cool storage of antecrysts formed as part of the same magmatic  
713 event, as persistent sill intrusion at the top of the magma reservoir causes the melt layer to migrate  
714 upwards and form in the overlying crust (e.g. Extended Data Figure 9c,d). The crystals here are rapidly  
715 mobilized by the arrival of the melt layer, but the history of the crystals and their genetic relationship  
716 with the magmatic event may be much more complex. However, simple over-accretion requires the  
717 magma supplying each sill to pass through the mush reservoir regardless of local melt fraction,  
718 rheology or density, which is inconsistent with available evidence and models.<sup>67,68</sup> We argue that our  
719 sill intrusion model better captures the effect of the local mush state on intrusion depth.

720

#### 721 **Sensitivity analysis**

722 Extended Data Table 1 shows that crustal magma reservoirs are described by a broad range of material  
723 properties. Values of many of these are poorly constrained. A simple sensitivity analysis was used to  
724 confirm that the results obtained are typical.

725 Previous work has shown that solutions to equations (1) – (5) are largely dictated by the value of  
726 the dimensionless scaling factor  $\kappa$ .<sup>51,71</sup> The effect of varying the other dimensionless parameter  $Ste$  is  
727 much smaller. Other studies, confirmed by additional numerical experiments conducted here, have  
728 shown that, for a given depth of intrusion and initial geothermal gradient, the thermal impact of  
729 intruding sills is controlled by the intrusion rate, irrespective of the model used to choose the sill  
730 intrusion depth.<sup>22,23,32,33</sup> The chosen intrusion rate of 5mm·yr<sup>-1</sup> for the example results shown here  
731 corresponds to the time-averaged magma productivity in arc settings simplified to a 1D geometry.<sup>24</sup>  
732 We now explore a range of intrusion rates around this value, consistent with estimates for different  
733 crustal magmatic systems and previous studies.<sup>21-24,32-34</sup>

734 A simple Monte-Carlo analysis<sup>89</sup> shows that 90% of the calculated values of  $\kappa$  for typical crustal  
735 parameters lie within the range  $0.028 < \kappa < 2160$  ( $-1.55 < \log \kappa < 3.335$ ; see Extended Data Figure 10a).  
736 Numerical solutions were obtained for ten values of  $\log \kappa$  sampled evenly over this range in log space,

737 for a range of values of the sill intrusion rate, three different intrusion depths and basalt that is  
738 intruded to a maximum thickness of 20km (Extended Data Table 1). The results are summarized in  
739 Extended Data Fig. 10b,c by plotting the incubation time (the time required to reach the end of the  
740 incubation phase and produce a persistent mush reservoir; see Extended Data Figure 2b), the  
741 activation time (the time required to produce an active reservoir with a low crystallinity felsic magma  
742 layer; see Extended Data Figure 2b), the bulk composition of the mobile magmas (i.e. magmas with  
743 melt fraction  $>0.7$ ), and the 'cold storage time' of antecrysts at the top of the reservoir, as a function  
744 of sill intrusion rate for the different intrusion depths. The 'cold storage time' is the time elapsed  
745 between the last intrusion and the local melt fraction exceeding 0.7 at locations close to the top of  
746 the reservoir (see Fig. 2 and Extended Data Figures 6, 8). The cold storage time reflects the likely range  
747 of crystal ages in magmas that have achieved melt fractions exceeding 0.7.

748 The incubation time scales with the reciprocal of the intrusion rate squared  $q^{-2}$  (Extended Data Fig.  
749 10b). The same scaling has been obtained in previous, purely thermal, models of repetitive sill  
750 intrusion using a variety of intrusion depth schemes, showing that the incubation time is relatively  
751 insensitive to the details of sill intrusion.<sup>22,23,90</sup> Varying the value of  $\kappa$  over the range specified has a  
752 negligible impact on the incubation time, regardless of intrusion rate or depth, reflecting the relatively  
753 small range of uncertainty in thermal parameters such as thermal conductivity, specific heat capacity  
754 and latent heat (Extended Data Table 1).

755 The impact of varying  $\kappa$  on the accumulation time is more significant, especially at lower intrusion  
756 rates when the accumulation time may be several million years longer than the incubation time  
757 (Extended Data Fig. 10b). Longer incubation times are observed for large values of  $\kappa$  that correspond  
758 to larger values of the melt shear viscosity and smaller values of matrix grain size, and for small values  
759 of  $\kappa$  that correspond to large values of the matrix bulk viscosity (Extended Data Table 1). Nevertheless,  
760 the accumulation time is finite so long as the incubation time is reached within the maximum intruded  
761 thickness of basalt; in other words, the formation of a high melt fraction layer is inevitable, so long as  
762 a persistent mush reservoir is present.

763 The composition of the high melt fraction (eruptible) magma in the reservoir is always bimodal,  
764 irrespective of the value of  $\kappa$ , the intrusion rate or intrusion depth (Extended Data Fig. 10c). The  
765 magma in the intruded sills has a composition close to that of the intruding basalt, while the magma  
766 in the layer that accumulates at the top of the reservoir has an evolved (approximately eutectic)  
767 composition, consistent with the results shown earlier for specific cases (Figure 3; Extended Data  
768 Figure 7a).

769 The impact of varying  $\kappa$  on the cold storage time is more significant, as is the effect of intrusion  
770 rate (Extended Data Fig. 10c). Smaller cold storage times are observed for larger values of  $\kappa$  that  
771 correspond to larger values of the melt shear viscosity and smaller values of matrix grain size  
772 (Extended Data Table 1). Smaller cold storage times are also observed for higher intrusion rates,  
773 because evolution of the system as a whole occurs more rapidly. The cold storage time reflects the  
774 relative timing of sill intrusion relative to remobilization. Nevertheless, the cold storage time is always  
775 non-zero; in other words, some antecrysts are stored in a cold (or cool), non-eruptible state, prior to  
776 remobilization by reactive flow.

777

#### 778 **Code availability.**

779 The code (MUSHREACT) used to solve equations (1)-(5) and produce the results reported here is  
780 available from the corresponding author on request. The code is platform dependent and is not  
781 optimized or tested for broad distribution, but the methodology is described within the article and  
782 preceding studies.<sup>10,34</sup>

783

#### 784 **Data Availability Statement**

785 No original data are reported that were not created using the software code (MUSHREACT). Data  
786 can be recreated using the code.

787

788 **Supplementary References**

- 789 31. Hodge, D.S. Thermal model for origin of granitic batholiths. *Nature* **251**, 297-299 (1974).
- 790 32. Petford, N. & Gallagher, K. Partial melting of mafic (amphibolitic) lower crust by periodic influx of  
791 basaltic magma. *Earth and Planetary Science Letters* **193**, 483 (2001).
- 792 33. Dufek, J. & Bergantz, G. Lower Crustal Magma Genesis and Preservation: a Stochastic Framework  
793 for the Evaluation of Basalt–Crust Interaction, *Journal of Petrology* **46**, 2167-2195 (2005).
- 794 34. Solano, J.M.S., Jackson, M.D., Sparks, R.S.J., Blundy, J.D. & Annen, C. Melt Segregation in Deep  
795 Crustal Hot Zones: a Mechanism for Chemical Differentiation, Crustal Assimilation and the  
796 Formation of Evolved Magmas. *Journal of Petrology* **53**, 1999-2026 (2012).
- 797 35. Bowen, N.L. Evolution of the Igneous Rocks. Dover, New York. 2<sup>nd</sup> Edn. pp362 (1956).
- 798 36. Hallworth, M.A., Huppert, H.E., & Woods, A.W., Crystallization and layering induced by heating a  
799 reactive porous medium, *Geophysical Research Letters* **31**, L13605 (2004)
- 800 37. Kerr, R.C., Woods, A.W., Grae Worster, M. & Huppert, H.E., Disequilibrium and macrosegregation  
801 during solidification of a binary melt, *Nature* **340**, 357-362 (1989)
- 802 38. Heise, W. *et al.* Melt distribution beneath a young continental rift: The Taupo Volcanic Zone,  
803 New Zealand. *Geophys. Res. Lett.* **34**, L14313 (2007).
- 804 39. Bachmann, O. & Bergantz, G.W. On the origin of crystal-poor rhyolites: extracted from  
805 batholithic crystal mushes. *Journal of Petrology* **45**, 1565-1582 (2004).
- 806 40. Costa, A., Caricchi, L. and Bagdassarov, N. A model for the rheology of particle-bearing  
807 suspensions and partially molten rocks. *Geochemistry, Geophysics, Geosystems* **10**, Q03010,  
808 (2009).
- 809 41. Wolf, M.B. & Wyllie, P.J. Dehydration-melting of solid amphibolite at 10 kbar: Textural  
810 development, liquid interconnectivity and applications to the segregation of magmas.  
811 *Mineralogy and Petrology* **44**, 151–179 (1991).
- 812 42. Ducea, M.N., Otamendi, J., Bergantz, G.W., Jianu, D. & Petrescu, L., The origin and petrologic  
813 evolution of the Ordovician Famatinian-Puna arc, in DeCelles, P.G., et al., eds., Geodynamics of  
814 a Cordilleran orogenic system: The Central Andes of Argentina and northern Chile: *Geological*  
815 *Society of America Memoir* **212**, 125–138 (2015).
- 816 43. Yoshino T. & Okudaira T. Crustal growth by magmatic accretion constrained by metamorphic P-T  
817 paths and thermal models of the Kohistan arc, NW Himalayas. *J. Petrology* **45**(11), 2287–2302.  
818 (2004).
- 819 44. Hacker B.R., Mehl L., Kelemen P.B., Rioux M., Behn M.D. & Luffi P., Reconstruction of the  
820 Talkeetna intraoceanic arc of Alaska through thermobarometry. *J. Geophys Res.* **113**, B03204  
821 (2008).
- 822 45. Rosenberg, C.L. & Handy, M.R. Experimental deformation of partially melted granite revisited:  
823 implications for the continental crust. *Journal of Metamorphic Geology* **23**, 19 (2005).
- 824 46. Dell'Angelo, L.N., Tullis, J. & Yund, R.A. Transition from dislocation creep to melt-enhanced  
825 diffusion creep in fine-grained granitic aggregates. *Tectonophysics* **139**, 325–332 (1987).
- 826 47. Mei, S., Bai, W., Hiraga, T. & Kohlstedt, D.L. Influence of melt on the creep behavior of olivine-  
827 basalt aggregates under hydrous conditions. *Earth and Planetary Science Letters* **201**, 491–507  
828 (2002).
- 829 48. McKenzie, D.P. The generation and compaction of partially molten rock. *Journal of Petrology* **25**,  
830 713 (1984).
- 831 49. Richter, F.M. & McKenzie, D. Dynamical models for melt segregation from a deformable matrix:  
832 *The Journal of Geology* **92**, 729–740 (1984).
- 833 50. Connolly, J. A. D. & Podladchikov, Y. Y. Compaction driven fluid flow in viscoelastic rock.  
834 *Geodinamica Acta* **11**, 55-84 (1998).
- 835 51. Jackson, M.D., Cheadle, M.J. & Atherton, M.P. Quantitative modeling of granitic melt generation  
836 and segregation in the continental crust. *Journal of Geophysical Research* **108**, 2332-2353  
837 (2003).

- 838 52. Hersum, T.G., Marsh, B.D., and Simon, A.C. Contact partial melting of granitic country rock, melt  
839 segregation, and re-injection as dikes into ferrar dolerite sills, McMurdo dry valleys, Antarctica.  
840 *Journal of Petrology* **48**, 2125 (2007).
- 841 53. Jackson, M.D., Gallagher, K., Petford, N., and Cheadle, M.J., Towards a coupled physical and  
842 chemical model for tonalite–trondhjemite–granodiorite magma formation. *Lithos* **79**, 43 (2005).
- 843 54. Keller, T., Katz, R.F. and Hirschmann, M.M., Volatiles beneath mid-ocean ridges: Deep melting,  
844 channelised transport, focusing, and metasomatism, *Earth and Planetary Science Letters* **464**,  
845 55-68, 2017.
- 846 55. Katz, R.F. Magma dynamics with the enthalpy method: Benchmark solutions and magmatic  
847 focusing at mid-ocean ridges. *Journal of Petrology* **49**, 2099-2121 (2008).
- 848 56. Ranalli, G. *Rheology of the Earth: Deformation and flow processes in geophysics and geodynamics*  
849 (2<sup>nd</sup> Edn.), pp.366, Allen and Unwin, London, UK (1987).
- 850 57. Schmeling, H., Kruse, J.P. & Richard, G., Effective shear and bulk viscosity of partially molten rock  
851 based on elastic moduli theory of a fluid filled poroelastic medium, *Geophysical Journal*  
852 *International* **190**, 1571-1578 (2012).
- 853 58. Giordano, D., Russell, J. K. & Dingwell, D. B. Viscosity of magmatic liquids: A model. *Earth and*  
854 *Planetary Science Letters* **271**, 123-134 (2008).
- 855 59. Bercovici, D., Ricard, Y. & Schubert, G. A two-phase model for compaction and damage, part 1:  
856 General Theory: *Journal of Geophysical Research* **106**, 8887–8906 (2001).
- 857 60. Ricard, Y., Bercovici, D. & Schubert, G., A two-phase model for compaction and damage. 2.  
858 Applications to compaction, deformation and the role of interfacial surface tension. *Journal of*  
859 *Geophysical Research* **106**, 8907–8924 (2001).
- 860 61. Sramek, O., Ricard, Y. & Bercovici, D. Simultaneous melting and compaction in deformable two-  
861 phase media: *Geophysical Journal International* **168**, 964–982 (2007).
- 862 62. Simpson, G., Spiegelman, M. & Weinstein, M. I. A multiscale model of partial melts: 1. Effective  
863 equations. *Journal of Geophysical Research* **115**, B04410 (2010).
- 864 63. Khazan, Y. Melt segregation and matrix compaction: the mush continuity equation,  
865 compaction/segregation time, implications. *Geophysical Journal International* **183**, 601–610  
866 (2010).
- 867 64. Karlstrom, L., Dufek, J. & Manga, M., 2009, Magma chamber stability in arc and continental crust:  
868 *Journal of Volcanology and Geothermal Research* **190**, 249–270.
- 869 65. Parmigiani A., Faroughi S., Huber C., Bachmann O. & Su Y., Bubble accumulation and its role in  
870 the evolution of magma reservoirs in the upper crust, *Nature* **532**, 492-495 (2016).
- 871 66. Huppert, H.E. & Woods, A.W., The role of volatiles in magma chamber dynamics, *Nature* **420**,  
872 493-495 (2002).
- 873 67. Menand, T., Physical controls and depth of emplacement of igneous bodies: A review,  
874 *Tectonophysics* **500**, 11-19 (2011).
- 875 68. Kavanagh, J.L., Boutelier, D. & Cruden, A.R., The mechanics of sill inception, propagation and  
876 growth: Experimental evidence for rapid reduction in magmatic overpressure, *Earth and*  
877 *Planetary Science Letters* **421**, 117-128 (2015).
- 878 69. Spiegelman, M., Kelemen, P. & Aharonov, E. Causes and consequences of flow organization  
879 during melt transport: the reaction infiltration instability in compactible media. *Journal of*  
880 *Geophysical Research* **106**, 2061–2077 (2001).
- 881 70. Liang, Y., Schiemenz, A., Hesse, M. A. & Parmentier, E. M. Waves, channels, and the preservation  
882 of chemical heterogeneities during melt migration in the mantle. *Geophysical Research Letters*  
883 **38**, L20308 (2011).
- 884 71. Jackson, M.D. & Cheadle, M.J. A continuum model for the transport of heat, mass and  
885 momentum in a deformable, multicomponent mush, undergoing solid-liquid phase change.  
886 *International Journal of Heat and Mass Transfer* **41**, 1035-1048 (1998).
- 887 72. Ghiorso, M. S., & Sack, R.O. Chemical mass transfer in magmatic processes IV. A revised and  
888 internally consistent thermodynamic model for the interpolation and extrapolation of liquid-

- 889 solid equilibria in magmatic systems at elevated temperatures and pressures: *Contributions to*  
890 *Mineralogy and Petrology* **119**, 197–212 (1995).
- 891 73. Vielzuf, D. & Montel, J.M., Partial melting of metagreywackes. Part I. Fluid-absent experiments  
892 and phase relationships, *Contrib. Mineral. Petrol.* **117**, 375-393 (1994).
- 893 74. Blatter, D.L., Sisson, T.W., & Ben Hankins, W., Crystallization of oxidized, moderately hydrous arc  
894 basalt at mid- to lower-crustal pressures: implications for andesite genesis, *Contrib. Mineral.*  
895 *Petrol.* **166**, 861-886 (2013).
- 896 75. Burgisser, A. & Bergantz, G.W., A rapid mechanism to remobilize and homogenize highly  
897 crystalline magma bodies, *Nature* **471**, 212-215 (2011).
- 898 76. Sinigoi, S., Quick, J.E., Mayer, A. & Demarchi, G., Density-controlled assimilation of underplated  
899 crust, Ivrea-Verbano Zone, Italy. *Earth and Planetary Science Letters* **129**, 183-191 (1995).
- 900 77. Murase, T. & McBirney, A.R., Properties of some common igneous rocks and their melts at high  
901 temperatures. *Geological Society of America Bulletin* **84**, 3563-3592 (1973).
- 902 78. Gibb, F.G.F & Henderson, C.M.B., Convection and crystal settling in sills, *Contrib. Mineral. Petrol.*  
903 **109**, 538-545 (1992)
- 904 79. Latypov, R. M. The origin of basic– ultrabasic sills with S-, D-, and I-shaped compositional profiles  
905 by in-situ crystallization of a single input of phenocryst-poor parental magma, *Journal of*  
906 *Petrology* **44**, 1619–1656 (2003).
- 907 80. Hildreth, W. & Moorbath, S. Crustal contributions to arc magmatism in the Andes of Central  
908 Chile. *Contrib. Mineral. Petrol.* **98**, 455 (1988).
- 909 81. Sisson, T.W., Salters V.J.M. & Larson P.B. Petrogenesis of Mount Rainier andesite: magma flux  
910 and geologic controls on the contrasting differentiation styles at stratovolcanoes of the  
911 southern Washington Cascades. *Geological Society of America Bulletin* **126**, 122-144 (2013).
- 912 82. Holness, M.B., Melt segregation from silicic mushes: a critical appraisal of possible mechanisms  
913 and their microstructural record, *Contributions to Mineralogy and Petrology* **173**, 48 (2018).
- 914 83. Philpotts A.R. & Dickson L.D. The formation of plagioclase chains during convective transfer in  
915 basaltic magma. *Nature* **406**, 59–61 (2000).
- 916 84. Castrucchio, A., Rust, A. & Sparks, R.S.J. Rheology and flow of crystal-rich bearing lavas: insights  
917 from analogue gravity currents, *Earth and Planetary Science Letters* **297**, 471-480 (2010).
- 918 85. Grae Worster, M., Huppert, H.E. & Sparks, R.S.J, Convection and crystallization in magma cooled  
919 from above, *Earth and Planetary Science Letters* **101**, 78-89 (1990).
- 920 86. Bergantz, G. W. & Dawes, R. Aspects of magma generation and ascent in continental lithosphere,  
921 in *Magmatic Systems*, edited by M. P. Ryan, chap. 13, Academic, San Diego, Calif., 1994.
- 922 87. Blatter, D.L., Sisson, T.W. & Ben Hankins, W. Voluminous arc dacites as amphibole reaction-  
923 boundary liquids, *Contrib. Mineral. Petrol.* **172**, 27 (2017).
- 924 88. Till, C.B., Vazquez, J.A. & Boyce, J.W., Months between rejuvenation and volcanic eruption at  
925 Yellowstone caldera, Wyoming, *Geology* **43**, 695-698 (2015).
- 926 89. Sobol, I.M., A Primer for the Monte Carlo Method, CRC Press, 1<sup>st</sup> edn., pp. 126 (1994).
- 927 90. Michel, C. & Jaupart, C., Ultra-rapid formation of large volumes of evolved magma, *Earth and*  
928 *Planetary Science Letters* **250**, 38-52 (2006).

929

### 930 **Extended Data Figure and Table Captions**

931

932 **Extended Data Figure 1 | Phase behaviour and compositions of the modelled system. a**, Static melt  
933 fraction versus temperature for the modelled basalt and crust, extracted from the binary phase  
934 diagram for the chosen initial bulk compositions. Also shown are experimental equilibrium  
935 melting/crystallization data for metagreywackes and basalt over the pressure range 400-  
936 900MPa.<sup>12,73,74</sup> Triangles denote data from ref. 73; circles data from ref. 74; squares data from ref. 12.  
937 Static melt fraction denotes the melt fraction obtained if there is no relative motion of melt and  
938 crystals, so the bulk composition remains constant. **b**, SiO<sub>2</sub> content versus temperature modelled

939 here. Also shown are experimental data corresponding to those shown in (a). **c**, Melt fraction versus  
940 temperature obtained from the numerical model (data extracted from Supplementary Video 1 at  
941 three snapshots in time (0.97Ma, 1.39Ma and 1.66Ma after the onset of sill intrusions) corresponding  
942 to Figure 1 and Extended Data Figure 3b. Reactive flow in the mush decouples temperature and melt  
943 fraction: high melt fraction can be found at low temperature where reactive melt flow has caused the  
944 bulk composition of the mush to evolve and *vice-versa*.

945 **Extended Data Figure 2 | Maximum melt fraction as a function of time.** **a**, following a single sill  
946 intrusion during the incubation period, and **b**, over the life of the reservoir. In **a**, the sill cools rapidly,  
947 with the melt fraction falling below 0.7 (i.e. the crystallinity exceeding 30%) within 63a after intrusion,  
948 and the sill solidifying within 225a. The sharp decrease in melt fraction prior to full solidification is  
949 physical and represents the arrival of the solidification front during crystallisation at the eutectic. In  
950 **b**, during the *incubation phase*, maximum melt fraction spikes after each sill intrusion, but decreases  
951 rapidly and falls to zero between sill intrusions. The incubation phase ends when the melt fraction  
952 remains greater than zero between sill intrusions. During the *growing phase*, the maximum melt  
953 fraction at the top of the mush reservoir increases in response to reactive flow of buoyant melt. Spikes  
954 in melt fraction correspond to ongoing sill intrusions deeper in the reservoir. Melt fraction at the top  
955 of the mush increases until, during the *active phase*, evolved, low crystallinity (<30%) magma is  
956 present which is likely to rapidly leave and ascend to shallower crustal levels. New sill intrusions cease  
957 and, sometime later, the melt fraction at the top of the mush also starts to decrease. Overall, the  
958 reservoir is cooling. This is the *waning phase*, at the end of which the reservoir has completely  
959 solidified. Data in both plots extracted from Supplementary Video 1.

960 **Extended Data Figure 3 | Snapshots showing temperature, melt fraction, bulk composition and**  
961 **incompatible trace element concentration as a function of depth through a crustal section at 18km**  
962 **during the incubation and waning phases of the reservoir** after **a**, 0.82Ma following the onset of sill  
963 intrusions and **b**, 1.66Ma. Snapshots are taken from Supplementary Video 1. At early times **a**, during  
964 the incubation phase, individual sills cool rapidly. During the growing phase (not shown here; see  
965 Figure 1a), a persistent magma reservoir forms but the melt fraction is low and relatively uniform.  
966 However, buoyant melt migrates upwards and begins to accumulate at the top of the reservoir. During  
967 the active phase (not shown here; see Figure 1b), a high melt fraction layer forms. At late times **b**,  
968 during the waning phase, sill intrusions cease and the mush cools and solidifies. Shaded area in all  
969 plots denotes the vertical extent of basalt intrusion at that time. Equivalent results for intrusion at  
970 10km depth are shown in Extended Data Fig. 4.

971 **Extended Data Figure 4 | Snapshots showing temperature, melt fraction, bulk composition and**  
972 **incompatible trace element concentration as a function of depth through a crustal section at 10km**  
973 **depth during the incubation and waning phases** after **a**, 0.82Ma following the onset of sill intrusions  
974 and **b**, 1.66Ma. Snapshots are taken from Supplementary Video 2. The results are qualitatively very  
975 similar to those obtained at 18km depth (Extended Data Figure 3). During the incubation phase **a**,  
976 individual sills cool rapidly. During the waning phase **b**, sill intrusions cease and the mush cools and  
977 solidifies. Shaded area in all plots denotes the vertical extent of basalt intrusion at that time.

978 **Extended Data Figure 5 | Snapshots showing temperature, melt fraction, bulk composition and**  
979 **incompatible trace element concentration as a function of depth through a crustal section at 10km**  
980 **depth during the growing and active phases** after **a**, 0.99Ma following the onset of sill intrusions and  
981 **b**, 1.39Ma. Snapshots are taken from Supplementary Video 2. The results are qualitatively very similar  
982 to those obtained at 18km depth (Figure 1). During the growing phase **a**, a persistent mush reservoir  
983 forms but the melt fraction is low. Buoyant melt migrates upwards and begins to accumulate at the  
984 top of the reservoir. During the active phase **b**, the accumulating melt forms a high melt fraction layer

985 containing mobile magma. The composition of the melt in the layer is evolved and enriched in  
986 incompatible trace elements. Elsewhere in the mush, the melt fraction remains low. Shaded area in  
987 all plots denotes the vertical extent of basalt intrusions at that time.

988 **Extended Data Figure 6 | Cold storage and rapid remobilization of magma in a reservoir at 10km**  
989 **depth.** Results are qualitatively very similar to those obtained at 18km depth (Figure 2). Plot **a** shows  
990 melt fraction as a function of depth at the first snapshot after remobilization at 10km (1.441Ma).  
991 Shaded area denotes intruded basalt. Reactive flow of buoyant melt produces a high melt fraction  
992 layer that migrates upwards. Plot **b** shows temperature and melt fraction as a function of time at a  
993 depth of 10km. Similar results are obtained over the depth range 10-10.5km. Early sill intrusions  
994 rapidly cool and crystallize. The crystals are kept in 'cold storage' at sub-solidus temperature, but the  
995 temperature gradually increases in response to sill intrusions deeper in the reservoir. Soon (<0.3ka)  
996 after the temperature exceeds the solidus, the high melt fraction layer arrives at this depth and the  
997 reservoir is remobilized: the melt fraction increases rapidly to form a low crystallinity magma. The  
998 melt fraction increases much more rapidly and to a higher value than would be possible by melting  
999 alone. Plot **c** shows temperature and melt fraction as a function of time at a depth of 12km. Similar  
1000 results are obtained over the depth range 10.5-15km. Melt fraction remains low because reactive flow  
1001 has left a refractory residue at this depth. There is no remobilization, despite the increase in  
1002 temperature. Data extracted from Supplementary Video 2.

1003 **Extended Data Figure 7 | Geochemical consequences of reactive melt flow in crustal magma**  
1004 **reservoirs at 10km depth** created by intrusion of **(a)** mafic sills and **(b)** intermediate sills. Both plots  
1005 show SiO<sub>2</sub> content of low crystallinity (crystal fraction <30%) magmas. Solid curves show bulk magma  
1006 composition (melt plus crystals); dashed curves show melt composition alone. The peak at low SiO<sub>2</sub>  
1007 corresponds to magma within the intruding sills; the peak at high SiO<sub>2</sub> corresponds to magma within  
1008 high melt fraction layers near the top of the reservoir. In plot (a), measured data from the Snake River  
1009 Plain are shown for comparison;<sup>29</sup> the bimodality is clear although the basalt has a lower SiO<sub>2</sub> content  
1010 than modelled here. Bimodal compositions correspond to (1) the magma intruded into the reservoir,  
1011 and (2) the most evolved composition obtained by differentiation.

1012 **Extended Data Figure 8 | Cool storage and rapid remobilization of magma in a reservoir created by**  
1013 **intrusion of intermediate magma at 10km depth.** Results are qualitatively similar to those obtained  
1014 by intruding basalt magma. Plot **a** shows melt fraction as a function of depth at the first snapshot  
1015 after remobilization at a depth of 11.4km (1.28Ma). Reactive flow of evolved, buoyant melt produces  
1016 a high melt fraction layer that migrates upwards. Plot **b** shows temperature and melt fraction as a  
1017 function of time at a depth of 11.4km. Early sill intrusions rapidly cool and crystallize. The crystals are  
1018 kept in 'cool storage' at near-solidus temperature. At 1.28Ma, the high melt fraction layer arrives at  
1019 this depth and the reservoir is remobilized: the melt fraction increases rapidly to form a low  
1020 crystallinity magma. The melt fraction increases much more rapidly and to a higher value than would  
1021 be possible by melting alone. Melt fraction deeper in the reservoir remains low because reactive flow  
1022 has left a refractory residue at this depth.

1023 **Extended Data Figure 9 | Consequences of emplacement during (a, b) under-accretion and (c, d)**  
1024 **over-accretion.** During under-accretion, plot **a** shows melt fraction as a function of depth at the first  
1025 snapshot after remobilization at a depth of 22km (1.02Ma). Reactive flow of evolved, buoyant melt  
1026 produces a high melt fraction layer that migrates upwards. Plot **b** shows temperature and melt  
1027 fraction as a function of time at a depth of 22km. Similar results are obtained over the depth range  
1028 22-22.5km. Under-accretion causes the sill intrusion depth to progressively increase from 18km; in  
1029 this case, an intrusion at 22km occurs at 0.75Ma that rapidly cools and crystallises. The crystals are  
1030 kept in 'cool storage' at close-to-solidus temperature. At 1.02Ma the high melt fraction layer arrives

1031 at this depth and the reservoir is remobilized. During over-accretion, plot **c** shows melt fraction as a  
1032 function of depth at a snapshot in time (1.53Ma). In this case, the high melt fraction layer has migrated  
1033 into the overlying country rock. Plot **d** shows temperature and melt fraction as a function of time at a  
1034 depth of 17.5km, close to the top of the active magma reservoir. Similar results are obtained over the  
1035 depth range 17.5-18km. Crystals in the magma are sourced from the country rock and may be  
1036 genetically unrelated to the melt. There is no cold storage of crystals brought into the reservoir by  
1037 basaltic sill intrusions, as intrusion occurs deeper in the reservoir. In plots a and c, the shaded area  
1038 denotes intruded basalt.

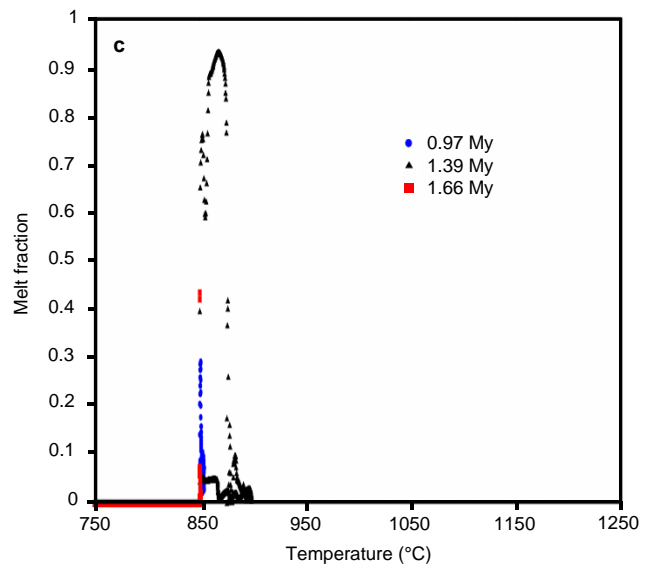
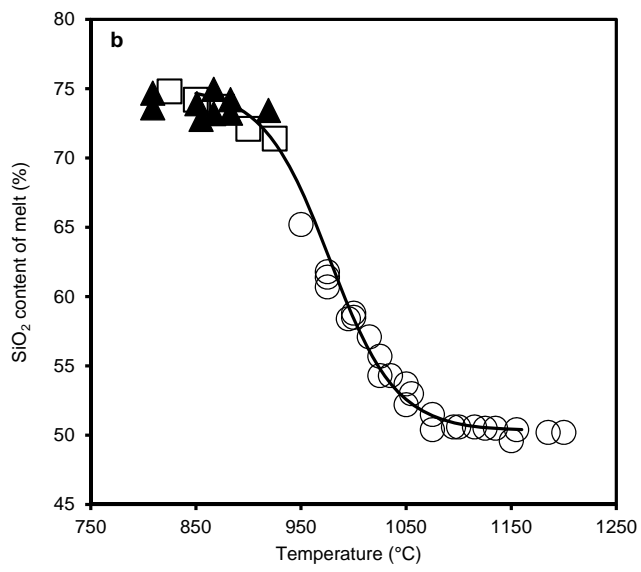
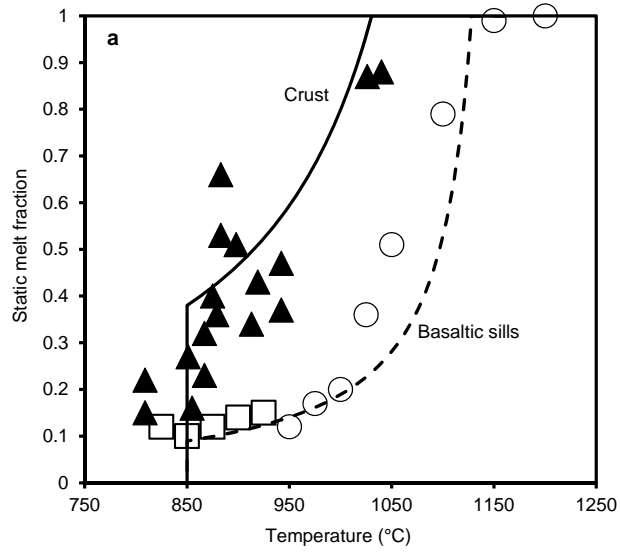
1039 **Extended Data Figure 10 | Sensitivity analysis.** Plot (a) is a frequency plot showing values of the  
1040 dimensionless scaling factor  $\kappa$  calculated using equation (12). Values of the input values were varied  
1041 uniformly over the range given in Extended Data Table 1 in a simple Monte-Carlo analysis.<sup>89</sup> Plot (b)  
1042 shows incubation and activation time; plot (c) shows cold storage time and eruptible magma  
1043 composition. Error bars and shaded regions in (b) and (c) denote the effect of varying the  
1044 dimensionless scaling factor  $\kappa$  over the range  $0.028 < \kappa < 2160$ . Error bars on the incubation time are  
1045 within the symbol size. Dashed lines denote fit to the incubation time of the form  $q^{-2}$  where  $q$  is the  
1046 intrusion rate. Colours in (b) and (c) denote different initial emplacement depths of 10km, 18km and  
1047 30km. Models were run for a maximum 20km of intruded basalt.

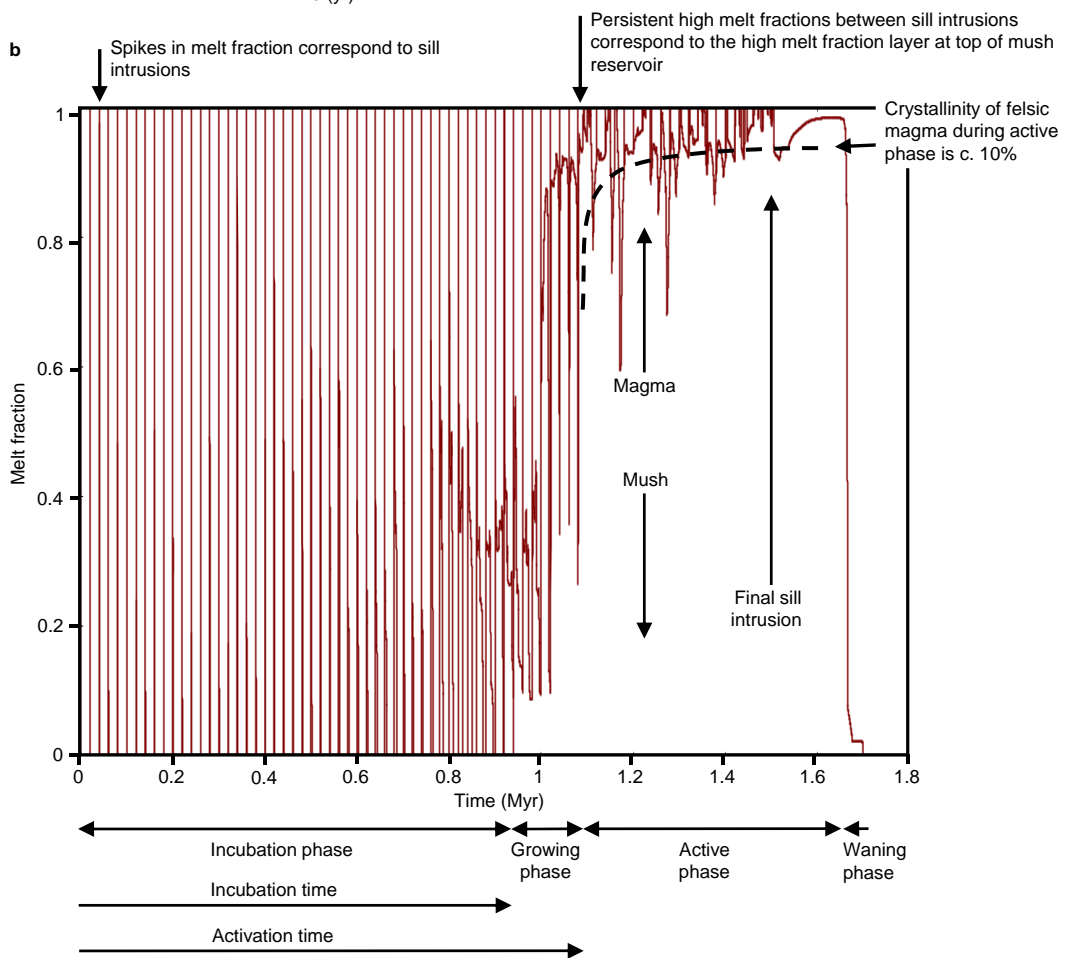
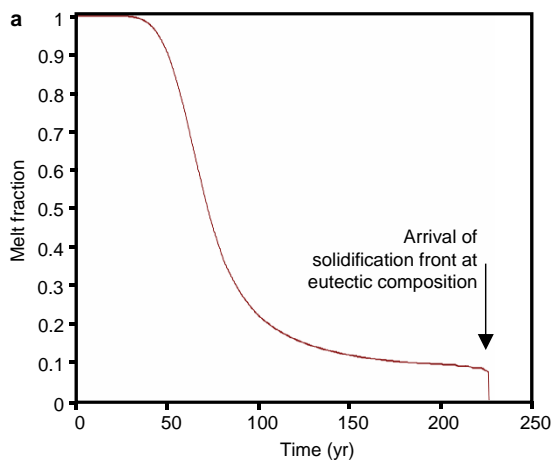
1048 **Extended Data Table 1 | Parameters used in the numerical experiments.** Values used to produce the  
1049 results shown in all figures except Extended Data Figure 10. A steeper geotherm suitable for thermally  
1050 mature crust<sup>23</sup> was assumed for the results shown in Extended Data Figures 4-8 which have intrusion  
1051 at 10km depth. The range of values for the sensitivity analysis was used to calculate the range of  
1052 values of the dimensionless scaling factor  $\kappa$  shown in Extended Data Figure 10a and produce the  
1053 associated numerical modelling results shown in Extended Data Figure 10b,c. Data sources are  
1054 indicated.

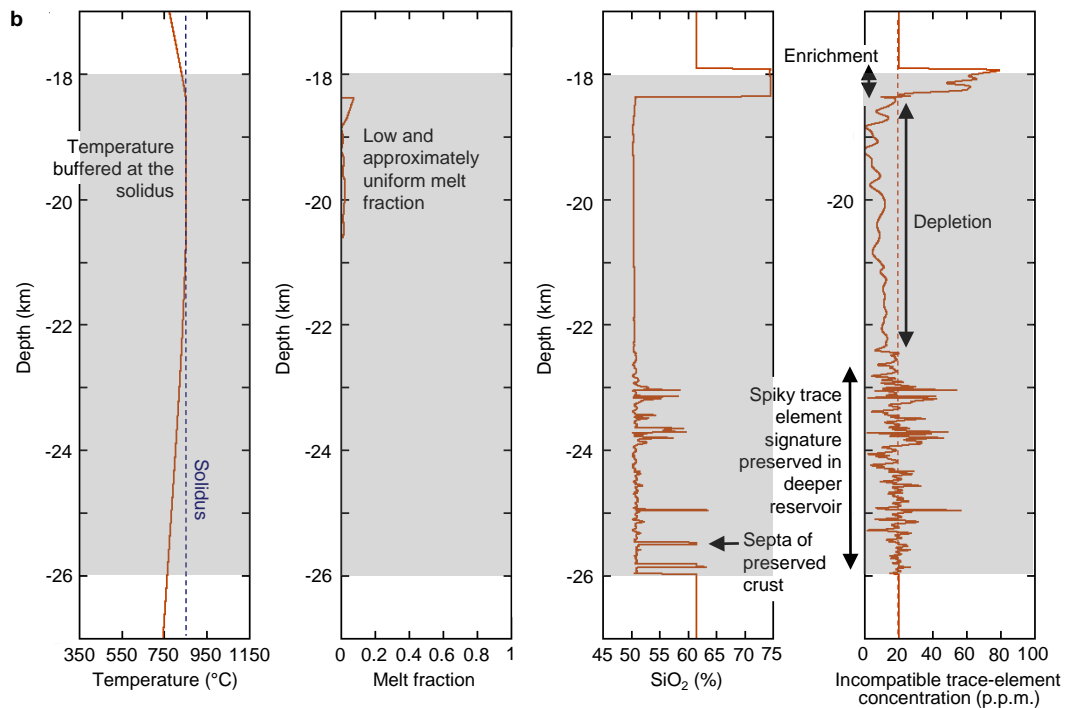
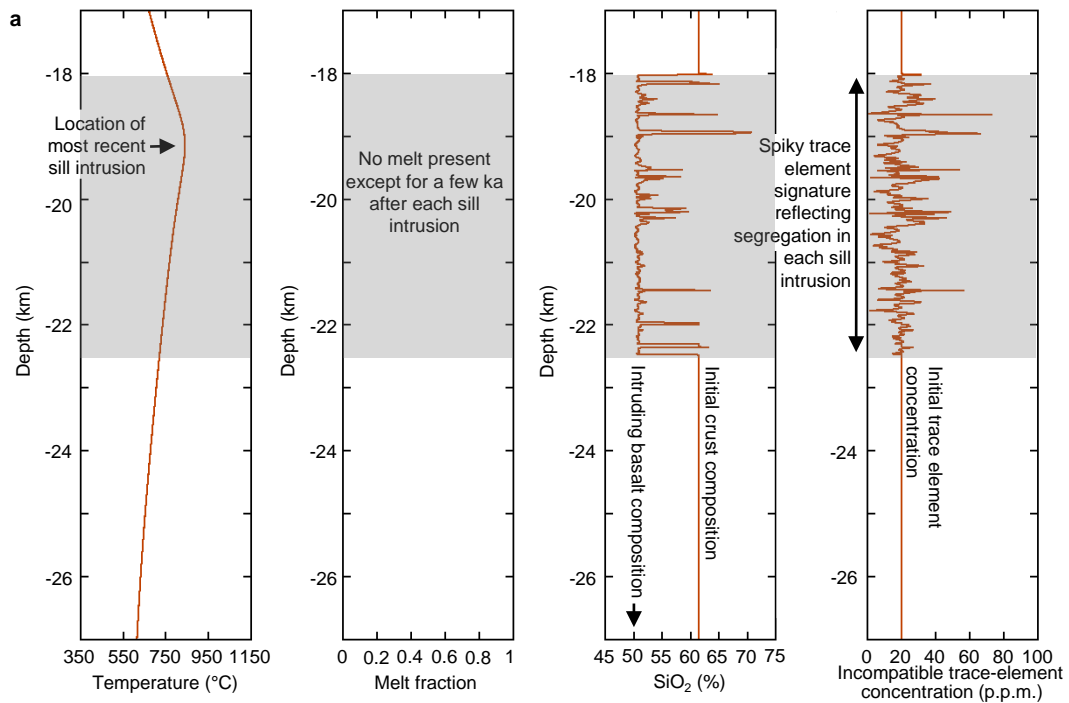
1055

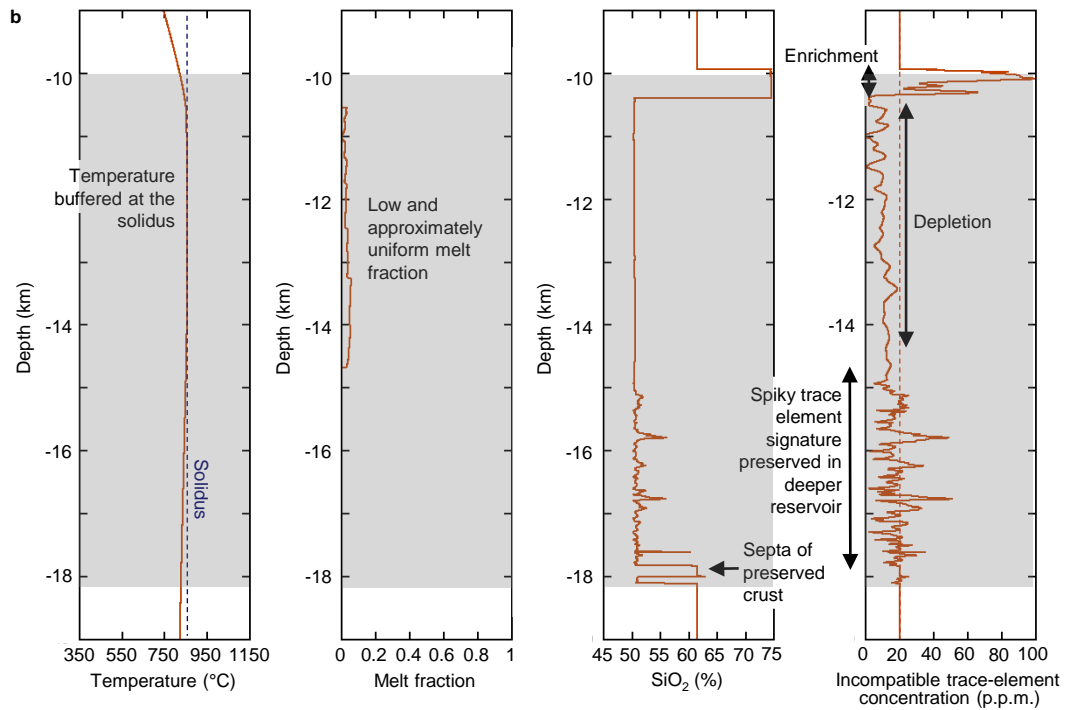
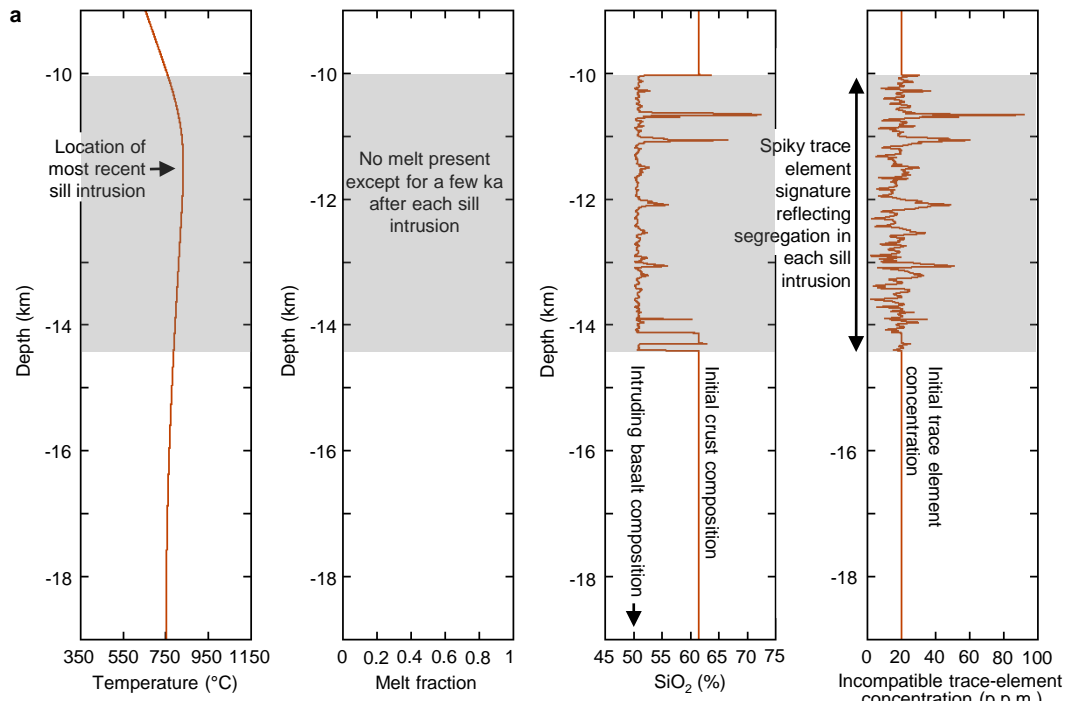
1056

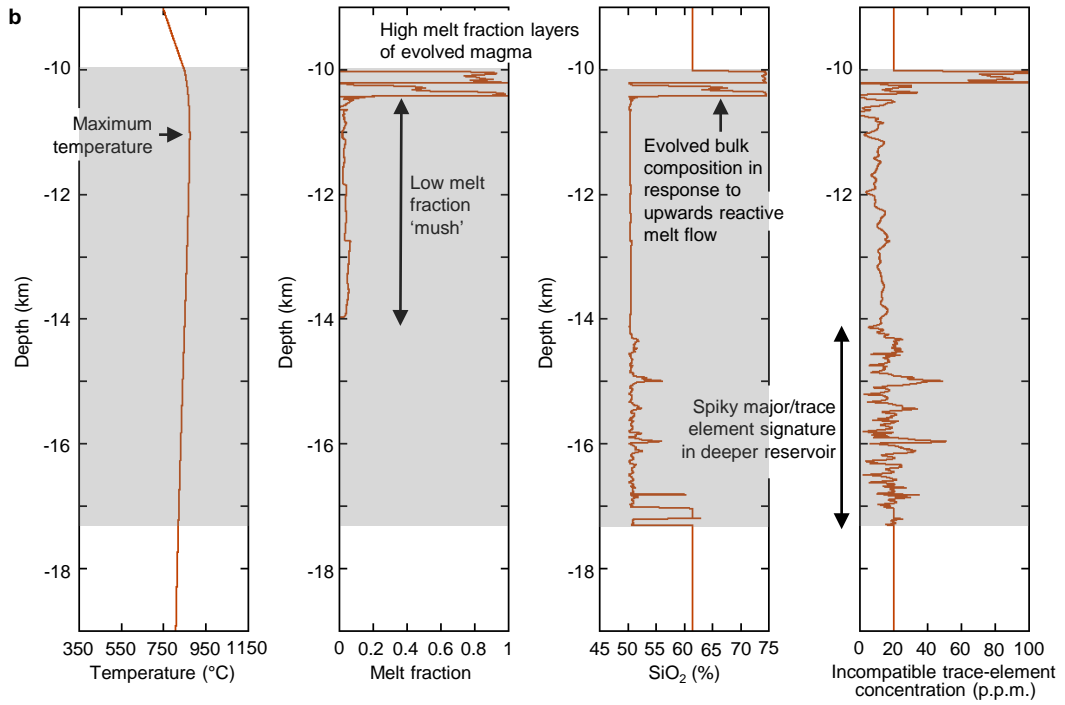
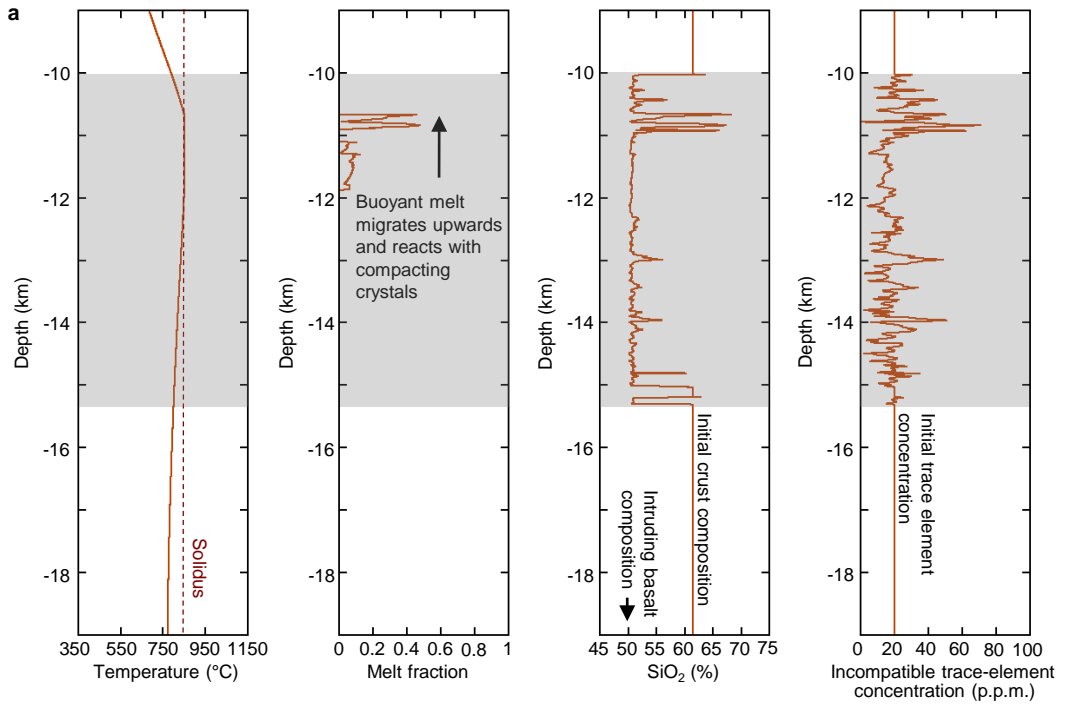


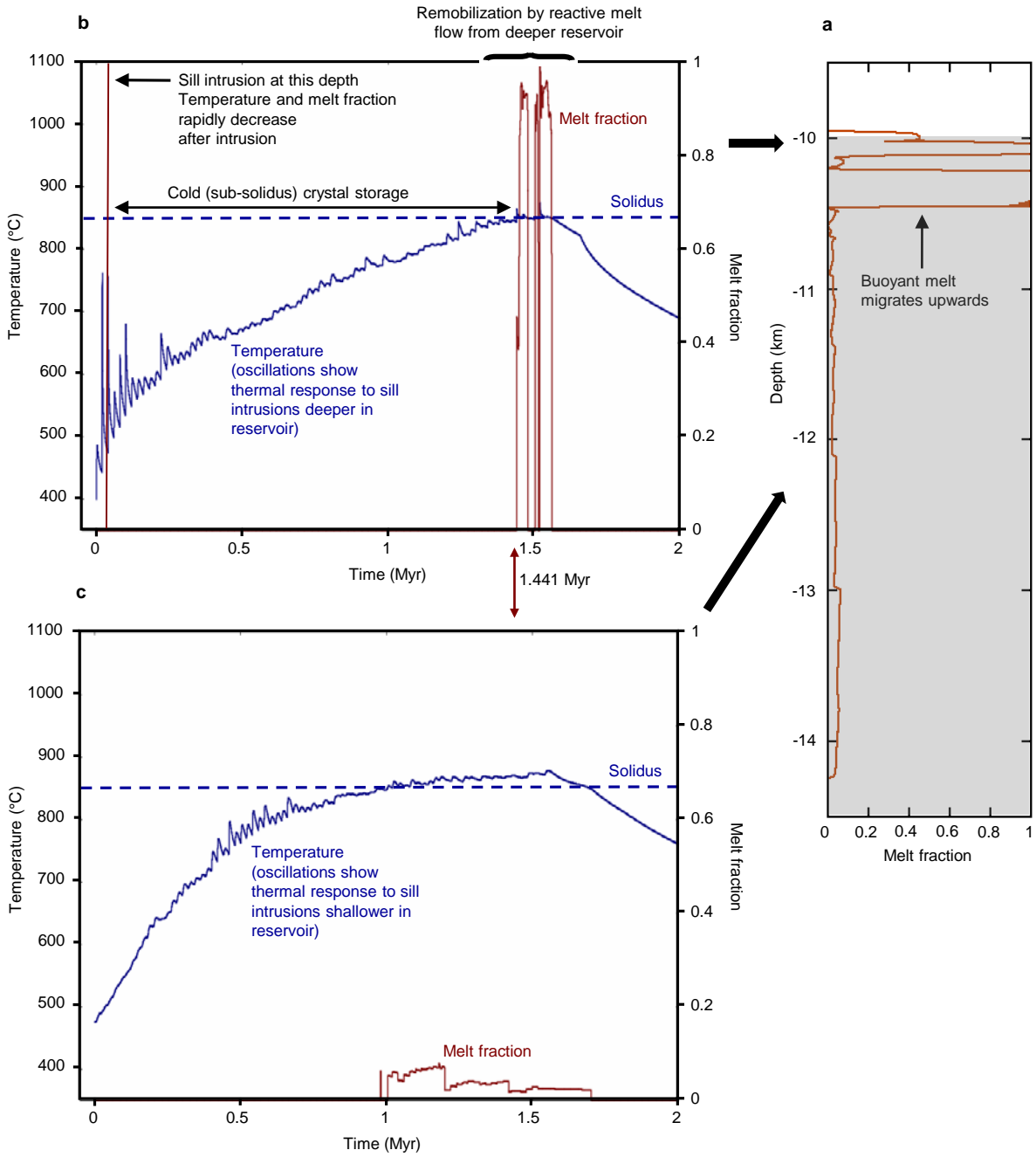


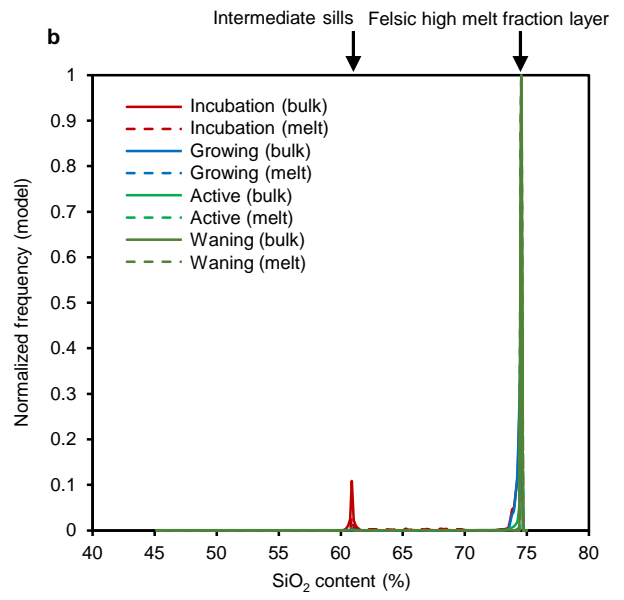
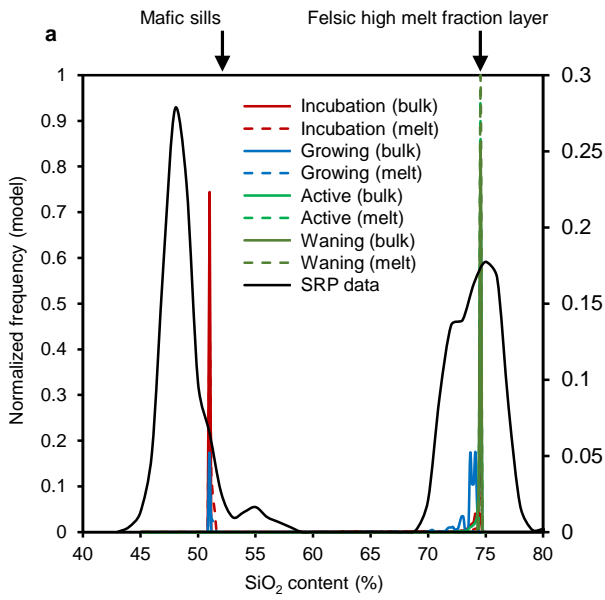


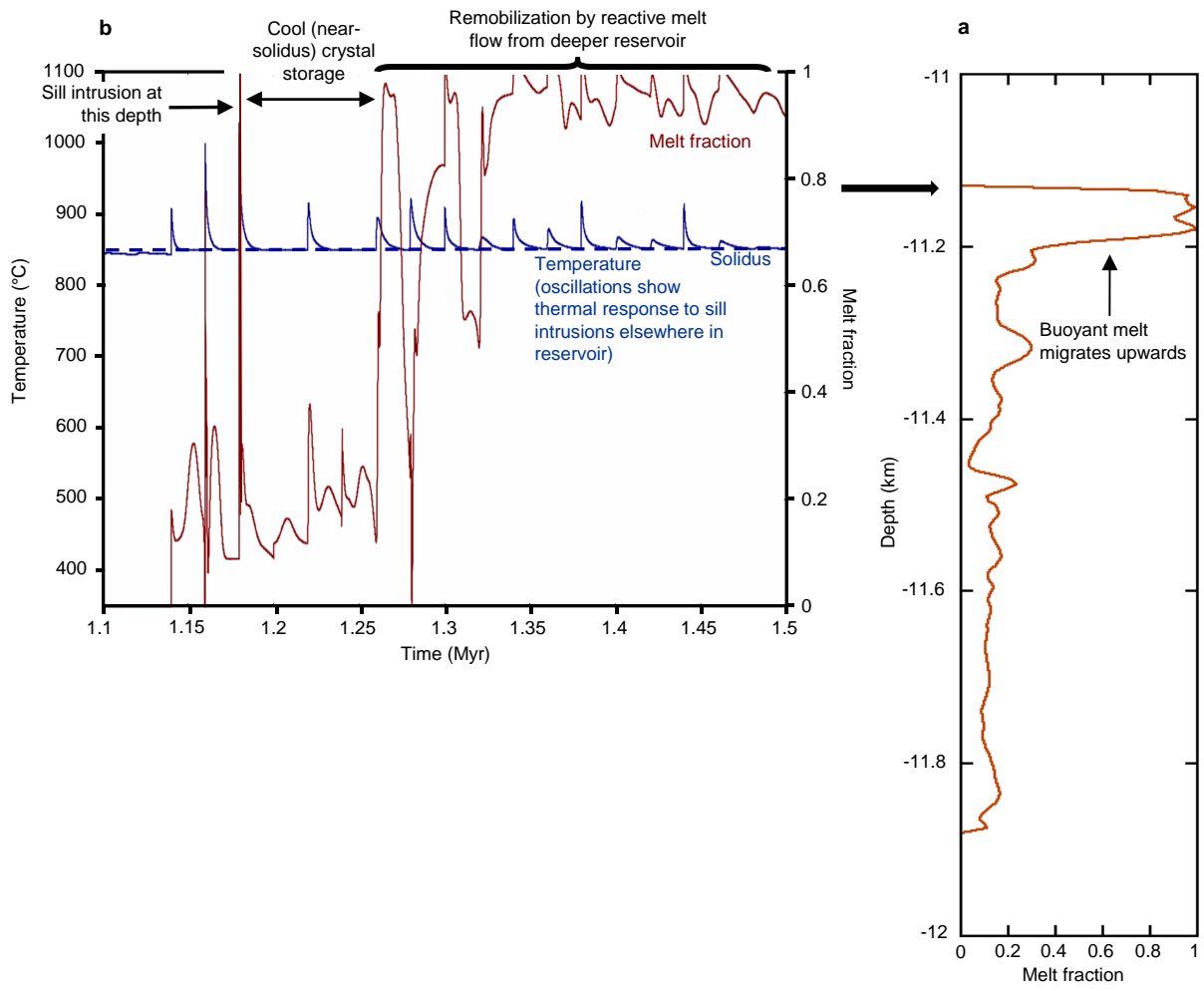




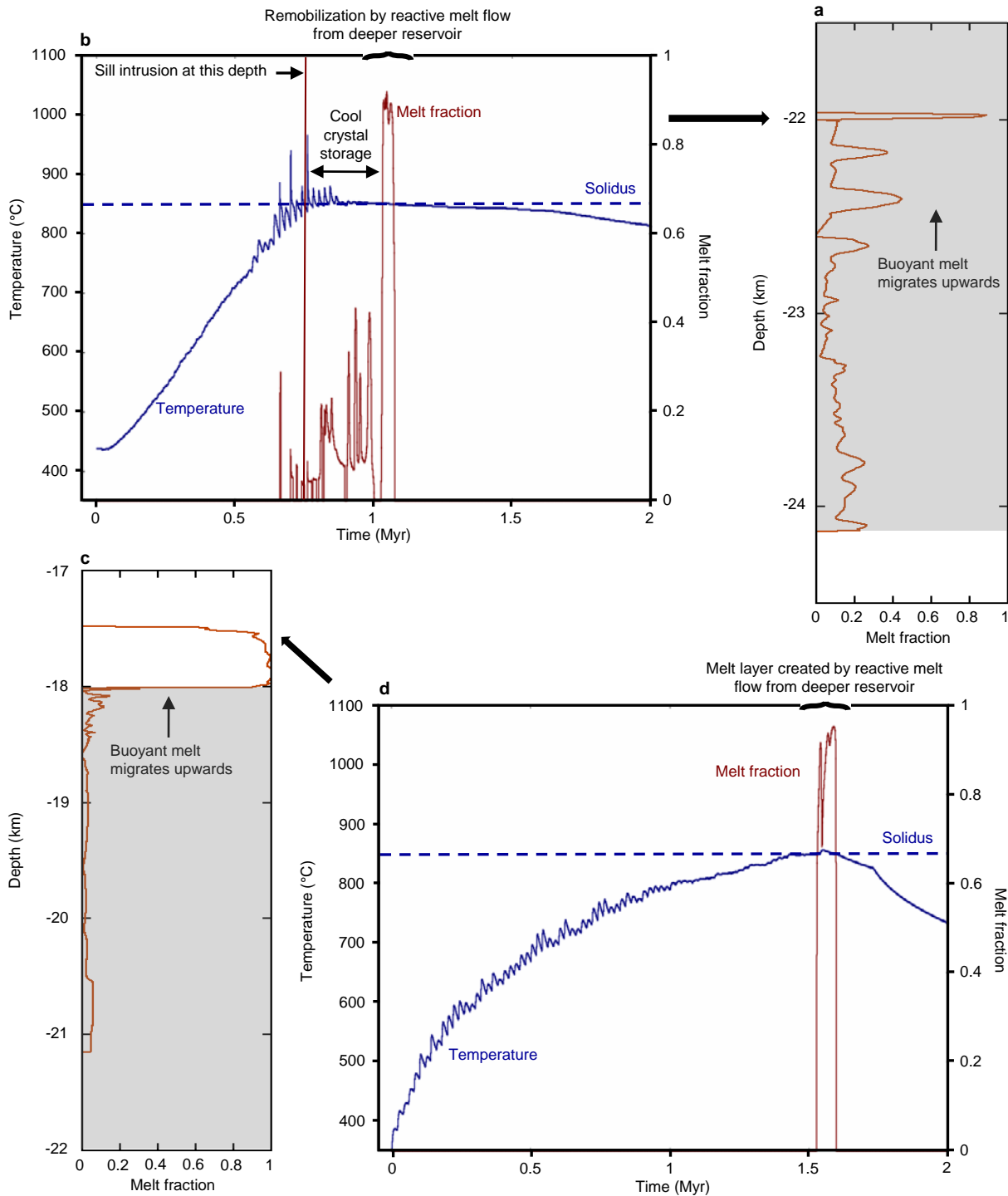


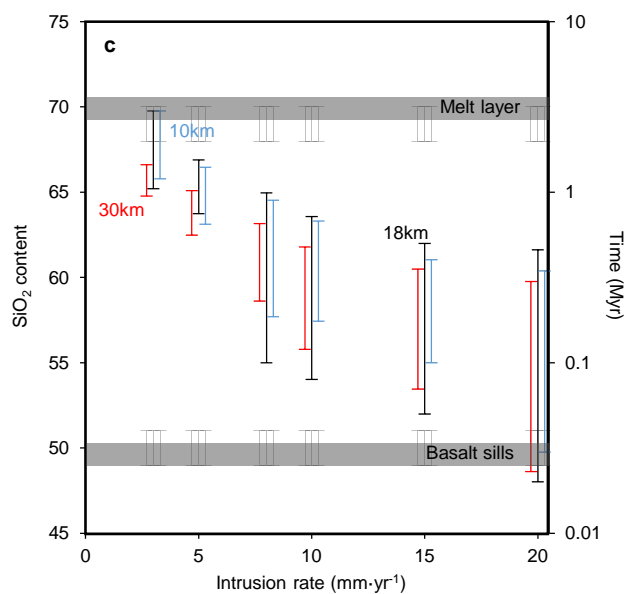
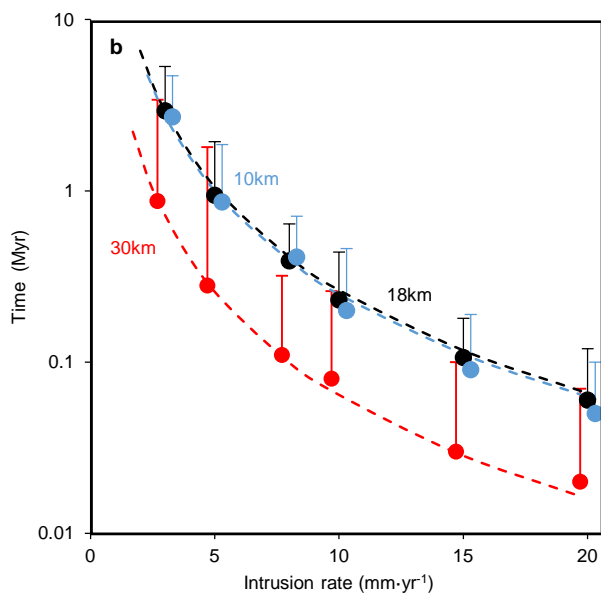
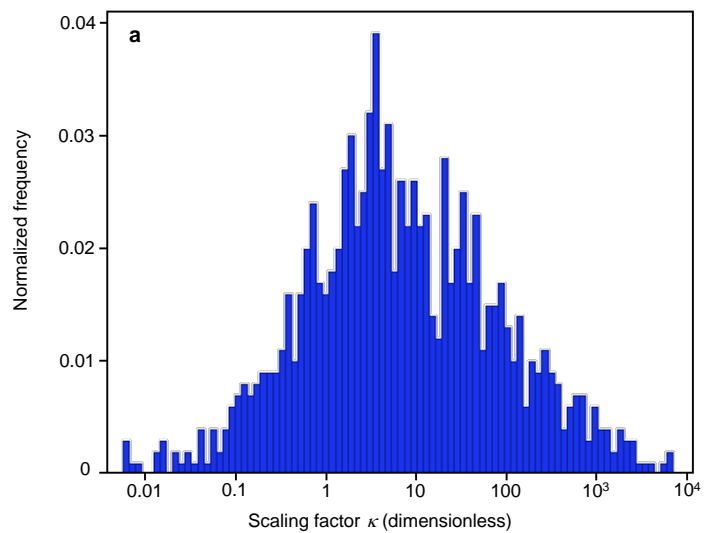


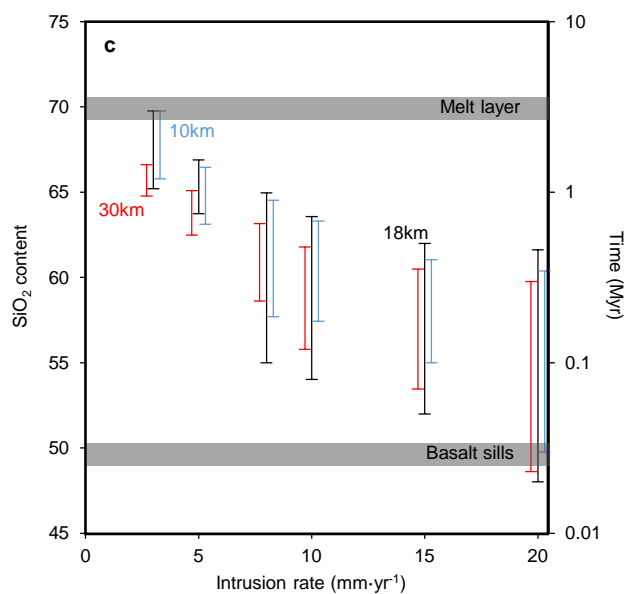
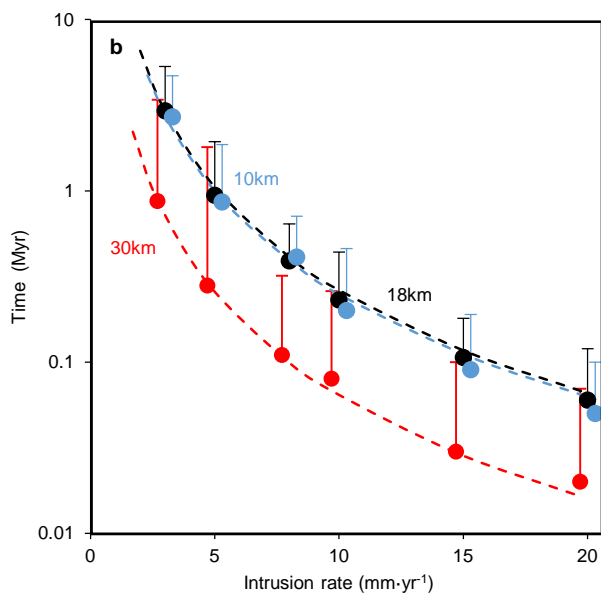
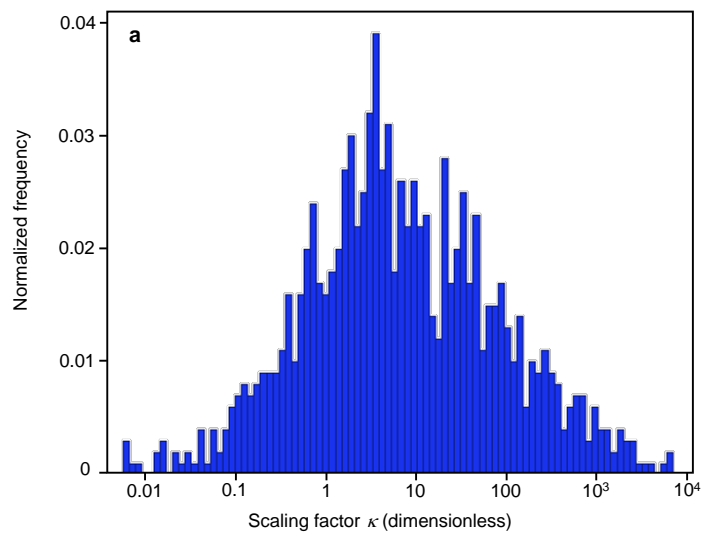












Symbol	Description and sources	Example case	Sensitivity analysis	Units
$k_T$	thermal conductivity <sup>22,23,33,51</sup>	3	1 - 3	W·°C <sup>-1</sup> ·m <sup>-1</sup>
$c_p$	specific heat capacity <sup>51</sup>	1100	1,020 - 1,220	J·kg <sup>-1</sup> ·°C <sup>-1</sup>
$L_i$	latent heat <sup>51</sup>	550000	400,000 - 600,000	J·kg <sup>-1</sup>
$T_L - T_S$	liquidus-solidus interval <sup>12,73,74</sup>	310	310	°C
$T_S$	solidus <sup>12,73,74</sup>	850	850	°C
$T_{geo}$	initial geotherm <sup>21-23,51</sup>	20	20, 40	°C·km <sup>-1</sup>
$a$	matrix grain radius <sup>51</sup>	$2.75 \times 10^{-3}$	$5 \times 10^{-4}$ - $5 \times 10^{-3}$	m
$\alpha$	permeability exponent <sup>51</sup>	3	3	None
$\beta$	bulk viscosity exponent <sup>51</sup>	0.5	0.5	None
$b$	permeability constant <sup>51</sup>	1/125	1/2500 - 1/50	None
$\mu_{max}$	shear viscosity of most evolved melt <sup>58</sup>	$10^5$	$10^4$ - $10^6$	Pa·s
$\mu_{min}$	shear viscosity of least evolved melt <sup>58</sup>	1	1	Pa·s
$\eta_r$	reference matrix shear viscosity <sup>26,50,51,57</sup>	$10^{15}$	$10^{14}$ - $10^{17}$	Pa·s
$q$	sill intrusion rate <sup>21-24,32-34</sup>	5	1 - 20	mm·yr <sup>-1</sup>
$Z_s$	sill thickness <sup>21-23,42</sup>	100	50-200	m
$a_1, a_2, a_3$	phase behavior parameters	50, -360, 1433.15	50, -360, 1433.15	°C
$a_4, a_5, a_6, a_7, a_8$	silica content modelling parameters	62.7, 12.38, -0.0158, 15.44	62.7, 12.38, -0.0158, 15.44	-
$\rho_r$	reference density <sup>77</sup>	2850	2850	kg·m <sup>-3</sup>
$\rho_{smin}$	density of most evolved solid composition <sup>25,76,77</sup>	3000	3000	kg·m <sup>-3</sup>
$\rho_{smax}$	density of least evolved solid composition <sup>25,76,77</sup>	2600	2600	kg·m <sup>-3</sup>
$\rho_{min}$	density of most evolved melt composition <sup>26,76,77</sup>	2880	2880	kg·m <sup>-3</sup>
$\rho_{max}$	density of least evolved melt composition <sup>25,76,77</sup>	2350	2350	kg·m <sup>-3</sup>
$S_{SiO_2}^{max}$	SiO <sub>2</sub> of most evolved composition <sup>12,73,74</sup>	75	75	%
$S_{SiO_2}^{min}$	SiO <sub>2</sub> of least evolved composition <sup>12,73,74</sup>	50	50	%
$K$	Trace element Nernst partition coefficient <sup>16</sup>	0.08	0.08	-